Untangling inconsistent magnetic polarity records through an integrated rock magnetic analysis: A case study on Neogene sections in East Timor

F. M. Aben[1,2], M. J. Dekkers[1], R. R. Bakker[1,3], D. J. J. van Hinsbergen[4], W. J. Zachariasse[4], G. W. Tate[5], N. McQuarrie[6], R. Harris[7], and B. Duffy[8]

[1]Paleomagnetic Laboratory Fort Hoofddijk, Utrecht University, Utrecht, Netherlands, [2]Now at University of Grenoble-Alpes, Grenoble CEDEX 9, France, [3]Department of Earth Sciences, ETH Zurich, Zurich, Switzerland, [4]Department of Earth Sciences, Utrecht University, Utrecht, Netherlands, [5]Geosciences, Princeton University, Princeton, New Jersey, USA, [6]Geology and Planetary Science, University of Pittsburgh, Pittsburgh, Pennsylvania, USA, [7]Department of Geological Sciences, Brigham Young University, Provo, Utah, USA, [8]Department of Geological Sciences, University of Canterbury, Christchurch, New Zealand

Abstract Inconsistent polarity patterns in sediments are a common problem in magnetostratigraphic and paleomagnetic research. Multiple magnetic mineral generations result in such remanence "haystacks." Here we test whether end-member modeling of isothermal remanent magnetization acquisition curves as a basis for an integrated rock magnetic and microscopic analysis is capable of isolating original magnetic polarity patterns. Uppermost Miocene-Pliocene deep-marine siliciclastics and limestones in East Timor, originally sampled to constrain the uplift history of the young Timor orogeny, serve as case study. An apparently straightforward polarity record was obtained that, however, proved impossible to reconcile with the associated biostratigraphy. Our analysis distinguished two magnetic end-members for each section, which result from various greigite suites and a detrital magnetite suite. The latter yields largely viscous remanence signals and is deemed unsuited. The greigite suites are late diagenetic in the Cailaco River section and early diagenetic, thus reliable, in the Viqueque Type section. By selecting reliable sample levels based on a quality index, a revised polarity pattern of the latter section is obtained: consistent with the biostratigraphy and unequivocally correlatable to the Geomagnetic Polarity Time Scale. Although the Cailaco River section lacks a reliable magnetostratigraphy, it does record a significant postremagnetization tectonic rotation. Our results shows that the application of well-designed rock magnetic research, based on the end-member model and integrated with microscopy and paleomagnetic data, can unravel complex and seemingly inconsistent polarity patterns. We recommend this approach to assess the veracity of the polarity of strata with complex magnetic mineralogy.

1. Introduction

Paleomagnetic analysis of rock units can provide key information on their age, through magnetostratigraphy, and on their paleogeographic position with respect to the dipole, provided these rocks carry an original primary magnetization. Establishing the timing of natural remanent magnetization acquisition in sedimentary records, however, is a common problem because of the potential of such rocks to be remagnetized [e.g., *Dekkers*, 2012; *Van Der Voo and Torsvik*, 2012]. When the natural remanent magnetization (NRM) is significantly younger than the actual depositional age of the sediments, we speak of remagnetization. Different remagnetization mechanisms for sedimentary rocks have been proposed, among which the most common are: (1) thermal resetting by prolonged exposure to temperatures lower than the unblocking temperature of the magnetic carrier (resulting in a thermoviscous remanent magnetization (TVRM)); (2) a secondary magnetic signal resulting from chemical addition of new magnetic carriers (resulting in a chemical remanent magnetization (CRM)); and (3) the oxidation or dissolution of the original primary carriers, the (fine-grained) remains then often carry a viscous remanent magnetization (VRM). Such remagnetized NRMs may coexist with the primary, or characteristic remanent magnetization (ChRM). It is crucial for any paleomagnetic study to evaluate these coexisting remanence signals and isolate the ChRM from remagnetized remanences.

All known magnetic carriers can be subject to remagnetization; many cases involving magnetite [e.g., *McCabe et al.*, 1983; *Meijers et al.*, 2011], hematite [e.g., *Van Der Voo and Torsvik*, 2012], or pyrrhotite [e.g., *Aubourg et al.*, 2012] have been reported. Further also the mineral greigite (Fe$_3$S$_4$), a common magnetic carrier in sedimentary rocks, is notorious for remagnetizations in marine sediments [e.g., *Jiang et al.*, 2001; *Sagnotti et al.*, 2005; *Rowan and Roberts*, 2006; *Lucifora et al.*, 2012].

In this paper, we report on paleomagnetic results obtained from an uppermost Miocene-Pliocene deep-marine sedimentary sequence [*Haig et al.*, 2012; *Nguyen et al.*, 2013] on the island of Timor in the Malay Archipelago. Two sedimentary sections were sampled for a biomagnetostratigraphic study aimed to establish uplift rates of the young Timor orogeny [*Tate et al.*, 2014]. We will show that among the dominant magnetic carriers are greigite and magnetite, and that a classic paleomagnetic directional analysis of these sections yields magnetic polarity patterns that are grossly inconsistent with biostratigraphic constraints. We use these sections as a case study to test a novel approach using end-member modeling based on rock magnetic research to unravel the inconsistent polarity pattern.

2. The Problem: Polarity Patterns Incompatible With Biostratigraphy

2.1. Geologic Setting and Sampling

The island of Timor has been subjected to folding, thrusting, and uplift since ∼10 Ma [*Harris*, 1991, 1992; *Haig and McCartain*, 2007; *Spakman and Hall*, 2010; *Fichtner et al.*, 2010; *Audley-Charles*, 2011] [*Tate et al.*, 2014] as a result of collision of overriding Banda oceanic lithosphere and overlying volcanic arc with the subducting continental margin of NW Australia. The downgoing Australian continental margin's upper crust contains two major sequences separated by a décollement horizon [*Carter et al.*, 1976; *Harris*, 1991; *Audley-Charles*, 2011] (Figure 1a): first, a Paleozoic-lower Mesozoic Gondwana "prerift to synrift" sequence (Gondwana megasequence) [*Carter et al.*, 1976] that formed prior to and during Jurassic extension along the northern Australian margin. Originally, this sequence was stratigraphically overlain by an upper Mesozoic-Cenozoic "postrift" sequence (Australian Continental Margin sequence). These two sequences became separated during late Neogene arc-continent collision along a décollement horizon, which offsets tectonic duplexes formed in both sequences. This décollement horizon was formed in a clay-rich horizon in the stratigraphy, and currently forms the Bobonaro tectonic mélange [*Harris et al.*, 1998]. Currently, the deformed Gondwana sequence is found in the north, and the deformed "postrift" sequence is found along the south coast and offshore southern Timor [*Harris*, 2011]. The Banda terrane is the highest tectonic unit on the island, found in thrust contact along the Bobonaro mélange with the Gondwana sequence as klippen in the central and northern parts of the island [*Harris*, 2006]. The studied sediments were deposited in synorogenic piggyback basins that occur in and occur in places where neither the Banda terrane nor the Australian Continental Margin sequence is present on this décollement. These sequences are filled with deep-marine (>2000 m) limestones at the base [*Audley-Charles*, 1986; *De Smet et al.*, 1990; *Haig and McCartain*, 2007; *Roosmawati and Harris*, 2009; *Haig*, 2012; *Tate et al.*, 2014] passing upward into pelagic marl and turbidite deposits [*Haig and McCartain*, 2007; *Nguyen et al.*, 2013]. These sediments form the Viqueque Formation and are presently found across the southern half of the island.

Emergence of Timor started around 4–3 Ma [*Audley-Charles*, 1986; *Harris*, 1991; *Haig and McCartain*, 2007; *Audley-Charles*, 2011; *Quigley et al.*, 2012; *Nguyen et al.*, 2013] and present-day altitudes approach 3 km. A detailed and reliable integrated biomagnetostratigraphic age model is vital to date the uplift evolution, and to this end, two sections covering the Viqueque Formation were sampled to determine the magnetic polarity pattern: the Cailaco River (CR) section and the Viqueque Type (VT) section (for detailed description, see *Tate et al.*, 2014). The Viqueque Type section is located in the southeast of Timor in a riverbed and is the stratigraphic type section of the Viqueque Formation, the Cailaco River section lies in a riverbed more inland in a separate basin [*Duffy et al.*, 2013].

The Viqueque Type section is a continuously exposed sequence of 240 m unconformably overlying the Bobonaro melange (Figure 2a). The base consists of deep-marine fossil-rich pelagic limestones, which grade into marls at 13 m from the base. An irregular alternation of mostly shales, turbiditic sandstones, and gravelly to conglomeratic debris-flow deposits is observed in the upper 190 m of the section [*Nguyen et al.*, 2013; *Tate et al.*, 2014]. No faults are observed and the bedding orientation is nearly constant, tilted to the Southeast by 20–30°. A foraminiferal biostratigraphy is published by *Haig and McCartain* [2007], and
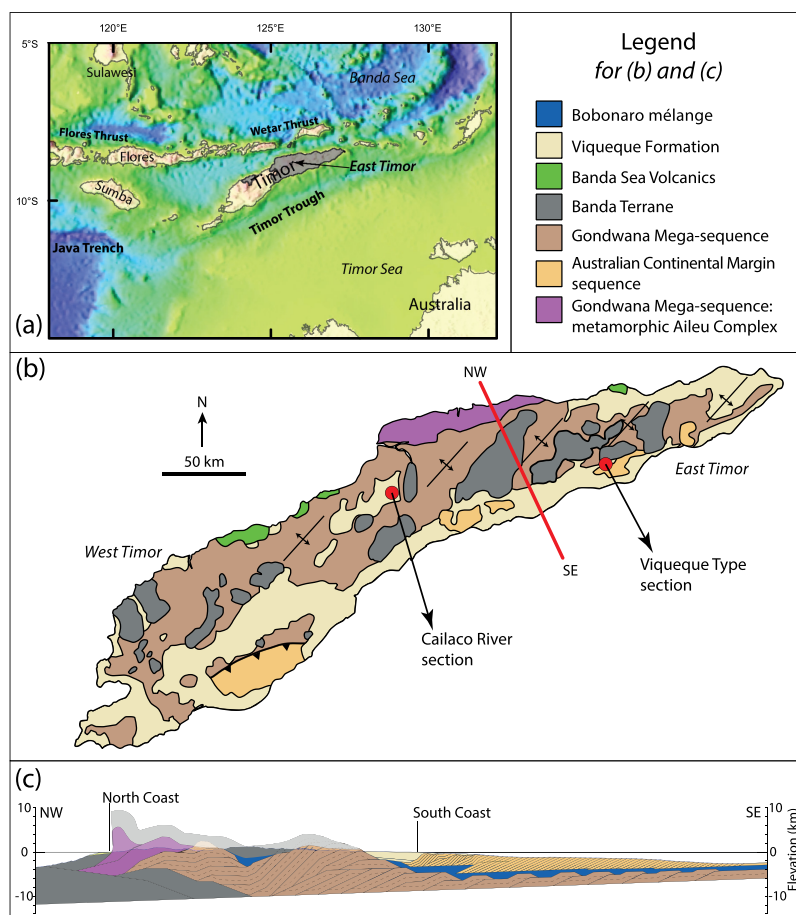
Figure 1. (a) Map showing the regional setting of Timor. The bathymetry clearly shows the main tectonic features such as the Java subduction trench, the shallower Timor through, and the continental margin of Australia in contact with the Banda-arc islands to the North. The country of East Timor is highlighted. Modified from *Tate et al.* [2014]. (b) Simplified geological map of Timor (modified from *Standley and Harris* [2009] and *Audley-Charles* [2011]) with the locations of the two sampled sections in the Viqueque formation. The red line indicates the location of the cross section in plot c. (c) Cross section running from Southwest to Northeast over East Timor, showing the complicated geology resulting from the arc-continent collision. The coastlines are indicated. Modified from *Tate et al.* [2014].

palynological results are reported by *Nguyen et al.* [2013]. A foraminiferal biostratigraphy based on the present sample set is reported in *Tate et al.* [2014]. A total of 122 levels were sampled for paleomagnetic research. Sample distance increases up-section in concert with an expected increase in sedimentation rate based on the lithology, to obtain a more or less equidistant sampling of time.

The Cailaco River section exposes ~500 m of irregularly exposed stratigraphy (Figure 2b). A similar lithological succession from pelagic limestones to marls is recognized up to the first nonexposed interval at 36 m from the base, followed by an irregular alteration of shales, turbiditic sandstones and debris-flow conglomerates to the top of the section. The foraminiferal biostratigraphy is reported in *Tate et al.* [2014]. In total, 120 levels were sampled for paleomagnetic research.

2.2. Classic Paleomagnetic Results

The classic, straightforward paleomagnetic analysis results in the large number of reversals for both sections as shown in Figure 2c (for detailed results, see supporting information A). For both sections the number of apparent polarity reversals far exceeds the number of reversals permitted by the biostratigraphic results. This disparity strongly suggests remagnetization of (parts of) both sections; the large number of reversals inferring locally remagnetized levels or at least several remagnetization events. Thermomagnetic runs and the strong gyroremnant magnetization (GRM) upon alternating field (AF) demagnetization point toward the presence of greigite as one of the magnetic carriers next to the expected detrital magnetic carriers. Greigite
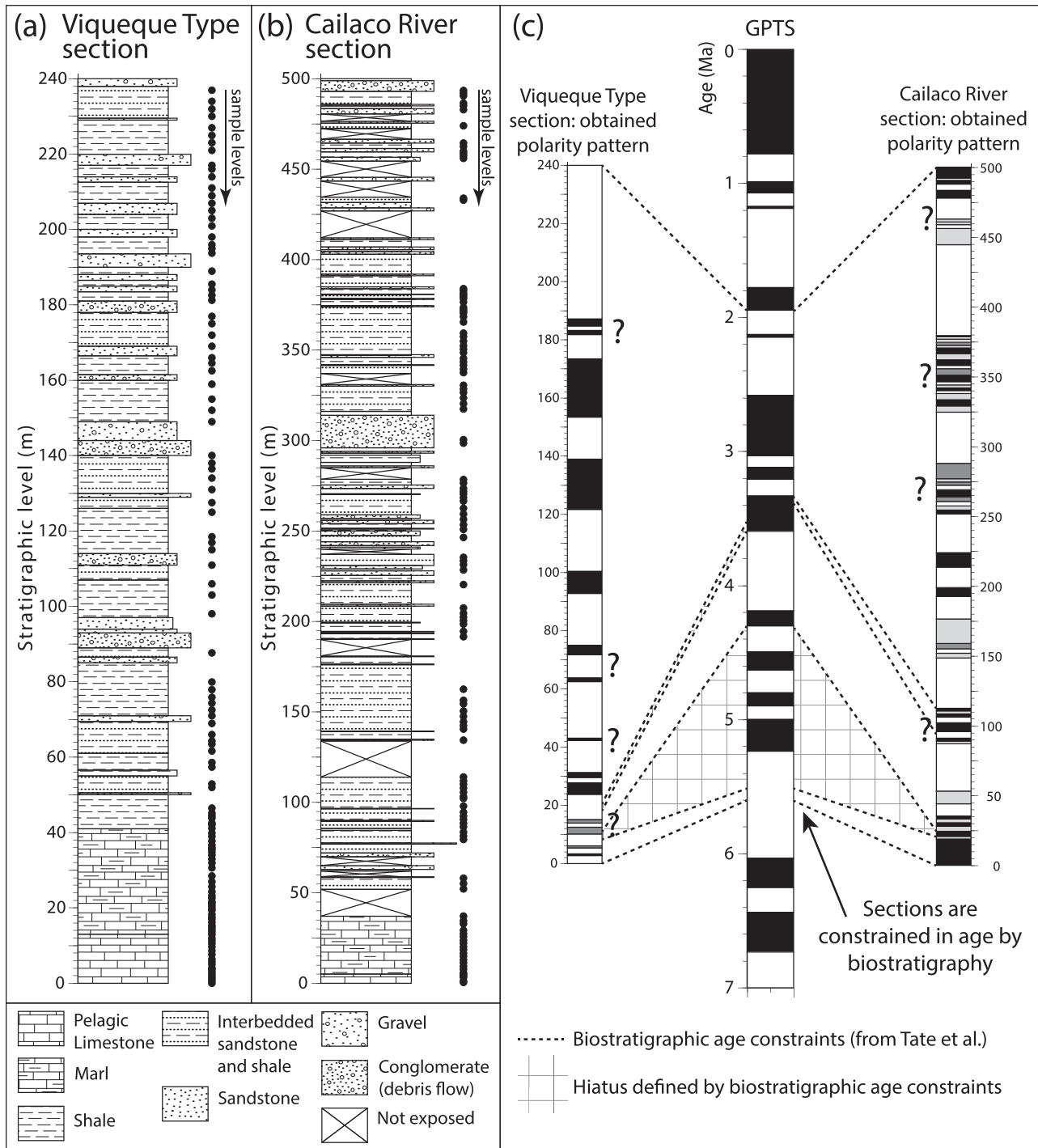
Figure 2. (a) Lithology of the Viqueque Type section including the paleomagnetic sample levels (black dots). Note the change from pelagic limestones and marls to turbidites at 40 m from the base of the section. (b) Lithology of the Cailaco River section. The same major transition in lithology is visible at 36 m from the base. Note the large number of unexposed intervals. (c) The resulting polarity patterns for (left) the Viqueque Type section and (right) the Cailaco River section, with the Geomagnetic Polarity Time Scale (GPTS; middle column). Biostratigraphic age constraints (short-dashed lines) from Tate et al. (2014). Gridded areas correspond to hiati, gray intervals represent unknown polarity. It is immediately clear that correlation of the sections' polarity pattern with the GPTS is impossible if the biostratigraphic age constraints are respected.

is a mineral that is often related to remagnetizations (see section 3). In the remainder of this paper, we assess whether it is possible to isolate remagnetized signals from original magnetizations and attempt to improve the polarity record of these sections.

3. Background: Greigite NRM and End-Member Modeling

Greigite was first recognized as precursor of pyrite in sulfate-reducing anoxic environments [*Berner*, 1984], and therefore long thought to be a very rare mineral. However, since the early 1990's greigite has been acknowledged as a common mineral in lacustrine [e.g., *Snowball and Thompson*, 1988, 1990a, 1990b] and marine deposits [e.g., *Giovanoli*, 1979; *Krs et al.*, 1992; *Roberts and Pillans*, 1993; *Florindo and Sagnotti*, 1995]. These marine records are often somehow remagnetized [e.g., *Jiang et al.*, 2001; *Sagnotti et al.*, 2005; *Rowan and Roberts*, 2006; *Lucifora et al.*, 2012] but can also give reliable results [e.g., *Roberts et al.*, 2005; *Vasiliev et al.*, 2007, 2008; *Hüsing et al.*, 2009].

It is its diagenetic formation, which always results in a CRM, that causes greigite's reputation of unreliable magnetic carrier. Different diagenetic processes can be responsible for greigite formation [see also *Roberts et al.*, 2011]. First, early diagenetic formation of greigite occurs in anoxic pore waters up to some meters below the sediment-water interface and is related to pyritization [*Berner*, 1984; *Benning et al.*, 2000; *Kao et al.*, 2004]. This CRM offsets and smoothens the paleomagnetic record by a variable time interval depending on sedimentation rate, varying between 100 kyr after deposition [*Rowan et al.*, 2009] to nearly syndepositional recording ages [*Hüsing et al.*, 2009]. Although this is the first greigite to form, "early" may thus still significantly postdate sedimentation. "Late" diagenetic greigite formation may result from different diagenetic processes, such as secondary growth of greigite on sheet silicates [*Canfield et al.*, 1992], on siderite [*Sagnotti et al.*, 2005] and on pyrite and gypsum [*Roberts and Weaver*, 2005]; such greigite may postdate sedimentation by (much) >100 kyr. Not all greigite is diagenetic, however: greigite magnetosomes produced by magnetotactic bacteria [*Mann et al.*, 1990; *Heywood et al.*, 1990; *Bazylinski et al.*, 1995] have been demonstrated to result in a syndepositional ChRM in some marine sedimentary records [*Vasiliev et al.*, 2008].

The different greigite formation processes, together with the presence of other magnetic carriers, can result in a remanence-"haystack" in marine sedimentary records. To unravel this, the paleomagnetic directional information can be subjected to methods such as fold tests [*McFadden*, 1990] or elongation/inclination correction [*Tauxe et al.*, 2008], which may demonstrate a precompaction, pretilting age of a remanence. These methods however are not always applicable because of lack of folding, noisy magnetic signals, or an insufficient amount of data records. In the Timorese sections the difference between greigite morphologies appears to be very subtle; analyses based on direction-independent rock magnetic properties or microscopy might be able to discriminate the greigite morphologies.

Direction-independent rock magnetic properties do have the discriminative power to recognize and isolate different populations of magnetic carriers, under the proviso that the primary ChRM and the secondary NRM reside in two distinctively different populations. Remagnetized rock records need not to be "binary" (one level remagnetized, one level not remagnetized) but likely will be a mixture of two (or more) remanence carriers.

It is therefore insightful to unmix the magnetic carriers into separate end-members of a chosen magnetic parameter and to evaluate the responsible formation processes of each end-member. The translation from end-member to formation process is achieved by a combination of rock magnetic properties, establishing the magnetic mineral species, the magnetic domain state, and microscopic observations constraining morphology and chemistry of each end-member. The last is especially important to distinguish between the different manifestations of greigite. With the mode of formation of the magnetic minerals known on a per sample basis, a paleomagnetic (re)interpretation can be made by discarding (part of) the remanence signals that are now considered suspect.

A suitable rock magnetic property to define end-members is the Isothermal Remanent Magnetization (IRM) acquisition curve for three main reasons. (i) They can be measured even on magnetically very weak specimens; (ii) They are not biased toward certain magnetic minerals; and (iii) are not very sensitive to (quasi) superparamagnetic (SP) contributions [*Heslop and Dillon*, 2007; *Dekkers*, 2012]. The separate coercivity components of an IRM-acquisition curve can be isolated by forward modeling or curve fitting [e.g., *Kruiver et al.*, 2001], which requires a priori knowledge about the magnetic carriers (and is laborious for a large sample collection). The fitting program constrains the fit by base functions; the resulting components are nonunique, and therefore potentially user sensitive. Instead of forward modeling, we use an inverse unmixing procedure developed by *Heslop and Dillon* [2007] based on an algorithm published by *Weltje* [1997]. The

procedure constrains end-members based on a large set of measured IRM-acquisition curves; it is less user-dependent and less laborious than curve fitting. The IRM-acquisition end-member model approach has been used before on magnetite-related remagnetizations [*Gong et al.*, 2009; *Van Hinsbergen et al.*, 2010; *Meijers et al.*, 2011] and for the budgeting of provenance areas [*Just et al.*, 2012a, 2012b]. For the first time, this approach will be used here for the reconstruction of a polarity pattern as well: it enables recognition of the sample levels containing remagnetized NRMs that can subsequently be discarded from interpretation.

4. Methodology

4.1. IRM-Acquisition End-Member Model

The unmixing algorithm is based on the assumption of linear mixing of end-members, which is justified for IRM acquisition curves [*Heslop and Dillon*, 2007]. Both the end-member compositions as well as the contribution of each end-member to a given measured curve are calculated from the set of IRM acquisition curves used as input. Mathematically, the linear mixing model is expressed as:

$$\mathbf{X} = \mathbf{MB} + \mathbf{E}$$

in which $\mathbf{X}$ is the compositional data matrix (n observations times p variables) and $\mathbf{M}$ contains the proportional contributions of the end-members to each observation. $\mathbf{B}$ contains the end-member compositions (q end-members times p variables) and $\mathbf{E}$ is the error matrix that contains nonsystematic contributions (such as instrumental noise). The bilinear mixing problem solves matrices $\mathbf{M}$, $\mathbf{B}$, and $\mathbf{E}$ without a priori knowledge of any of them. The algorithm by *Weltje* [1997] allows a trade-off between mathematical feasibility and geological realisticness by allowing minor violations of mathematical constraints (such as the nonnegative mixing constraint), making the model less sensitive to extreme outliers in the data set. The algorithm also causes the end-member compositions to stay reasonably close to the measured data, preventing the modeling of extreme end-member compositions. For mathematical details of the algorithms solution of the bilinear mixing problem, we refer to *Weltje* [1997] and *Heslop and Dillon* [2007].

The algorithm is incorporated into a MATLAB executable (see http://people.rses.anu.edu.au/heslop_d). The software normalizes the input curves to the highest IRM-value to produce a closed data set. Next, the systematic contribution to linear mixing is calculated for 2–9 end-members, including the coefficient of determination (r^2) between the actual measured data matrix and the ideal mixing representation. The break-in-slope in an r^2 versus number of end-members graph gives an indication for the optimal number of end-members. The steep slope segment represents gain in information upon increasing the number of end-members while the shallow slope segment is considered noise. After choosing the preferred number of end-members (user defined), the algorithm calculates the actual end-member compositions and their contributions to each input curve. A visual check of the end-member curves has shown to be useful; at first glance the end-member curve must be shaped as an IRM-acquisition curve. Although the mathematical solution of the algorithm is sound, it can produce (almost) similar end-member curves, which are not different from each other from a geological point of view. Producing end-member models with different numbers of end-members is recommended to monitor if and when similarities arise and end-members are being duplicated [*Dekkers*, 2012].

Pristine specimens of all sample levels of the Viqueque Type section and the Cailaco River section were subjected to IRM acquisition. Prior to IRM acquisition, all specimens were heated to 150°C to minimize the effects of oxidation rims around potentially present magnetite grains [*Van Velzen and Zijderveld*, 1995]. After the heating, the specimens were brought into the alternating field (AF) demagnetized state, proposed by *Heslop et al.* [2004] to minimize deviation of the IRM-acquisition curve from lognormality and to reduce the expression of possible magnetostatic interactions. This was achieved by exposing the specimens along three orthogonal axes in a 300 mT alternating field, performed with a laboratory-built AF-coil. IRM acquisition curves up to a peak field of 700 mT were obtained by measuring the IRM at 61 field levels (including the zero field), which were near-logarithmically distributed over the whole field range. The IRM acquisition was acquired with a custom-built robot that consists of a 2G Enterprises SQUID magnetometer (noise level 2–3 $\times$ 10^{-12} Am^2, weakest measured IRMs in the order of 10^{-8} Am^2), in line with a 2G Enterprises pulse magnetizer.

The unmixing algorithm dictates the input data to be monotonic, meaning that the IRM at a certain field is equal or higher than the IRM at the previous field. Therefore, the IRM acquisition curves were checked

interactively on nonmonotonic values and a visual check on the presence of so-called "staircase patterns" was applied as well. When noted, the data were smoothed; particular emphasis was paid to the 10–30 mT field interval that was measured in high resolution.

4.2. Supporting Rock Magnetic Research

To facilitate the interpretation of the end-members in terms of magnetic mineral suites and their formation processes, additional rock magnetic properties were measured on representative sample levels. These sample levels were chosen based on the results of the end-member model and include sample levels dominated by a single end-member as well as mixtures of end-members. Some high field thermomagnetic runs were performed on a custom-built horizontal translation Curie balance [*Mullender et al.*, 1993] with which the specimen's magnetization was measured up to 700°C, including various temperature loops during the heating trajectory to monitor possible irreversible behavior which indicates chemical alteration.

In thermomagnetic runs, neoformation of magnetic minerals (magnetite) obscures the analysis of originally present magnetic minerals in that temperature range. To establish the magnetic mineralogy at those higher temperatures, some samples were subjected to thermal demagnetization runs after application of a composite three-axial IRM [*Lowrie*, 1990]. The IRMs were induced with a PM4 pulse magnetizer (peak field reproducibility = 2 mT up to 130 mT, 0.02 T above 130 mT). The field strengths used are based on the IRM-acquisition curves of the end-members, so that each end-member's coercivity range is isolated on a single axis as much as possible, and are in decreasing order: 1.5 T, 300 mT, and 60 mT. Specimens were heated in the magnetically shielded oven mentioned before and measured on a JR6A AGICO spinner magnetometer (noise level 2.4 µA/m) using a four-position measurement protocol. Thirty-one thermal steps up to a peak temperature of 680°C were measured.

To further constrain the domain state and evaluate magnetostatic interactions of each end-member, major hysteresis loops and first-order reversal curve (FORC) diagrams were measured on the most representative sample levels. Small rock fragments were processed on an alternating gradient force magnetometer (Micro-Mag 2900, Princeton Measurements Corporation, noise level of 2×10^{-9} Am^2).

### 4.3. Optical Microscopy and Scanning Electron Microscopy

To evaluate visual trends between sample levels with different end-member contributions, optical microscopy (transmittent and reflected light) was applied to seven levels per section representing the full range of end-member contributions and lithologies. Special emphasis during this reconnaissance was on the most likely habitats for greigite and other possible magnetic minerals.

A scanning electron microscope (SEM; FEI-Company XL30-SFEG instrument) was used to visualize the morphologies of the magnetic end-members on the most representative samples. Energy-dispersive X-ray spectroscopy (EDS) was used to obtain semiquantitative standard-less chemical analysis. The principal difficulty to chemically demonstrate the presence of greigite (Fe_3S_4) is to distinguish it from other iron sulfides, mainly pyrite (FeS_2) and pyrrhotite (Fe_7S_8). Although the latter has a rather similar Fe:S ratio as greigite, these two minerals can be easily distinguished based on morphological features. This is not the case for pyrite and greigite, which have to be distinguished based on their Fe:S ratios. Due to the often small grain sizes the analytical volume of the electron beam at a standard energy level (e.g., 15 kV) can be too large, compromising the results. Therefore, we performed EDS spot-analyses with a 15 and 5 kV beam.

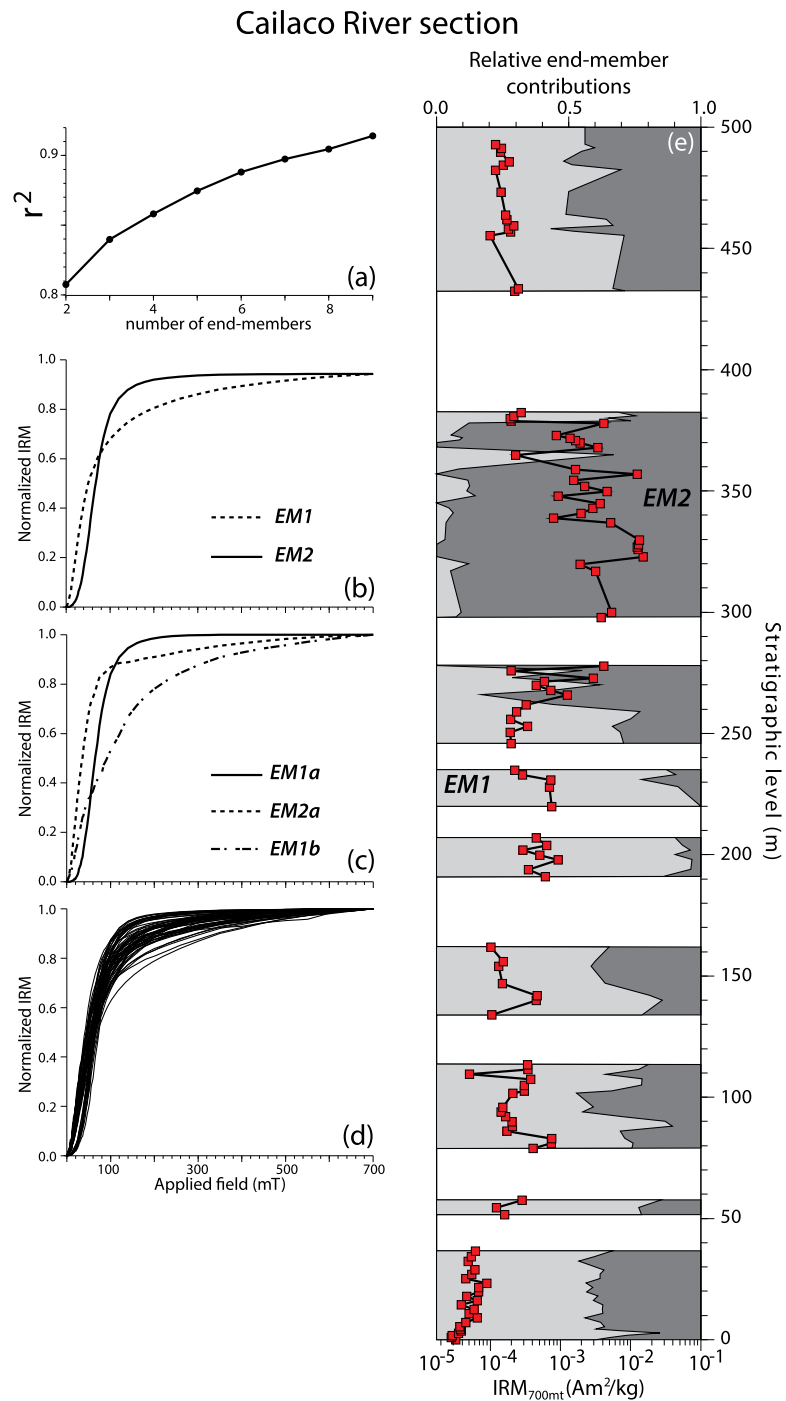## 5. Results

5.1. End-Member Modeling

For both sections, the unmixing algorithm mathematically suggests three end-members as the optimal number of end-members, based on the break-in-slope in the r^2 versus number of end-members graph (Figures 3a and 4a). End-member curves start to become noisy from four end-members upward. Since IRM acquisition curves are not noisy by nature the calculated "noise" is considered overinterpretation. Further, some end-members appear to be essentially duplicated: therefore, results from four end-members upward are regarded not to be representative. The end-member curves of the two and three end-member models show approximately the same shapes (Figures 3b, 3c, 4b, and 4c, input curves for reference in Figures 3d and 4d), indicated by the same line type of the curves. The sigmoidal end-member curves (called **EM2** and **EM2a**) are identical in both models, the other end-member curve from the two end-member model (**EM1**)
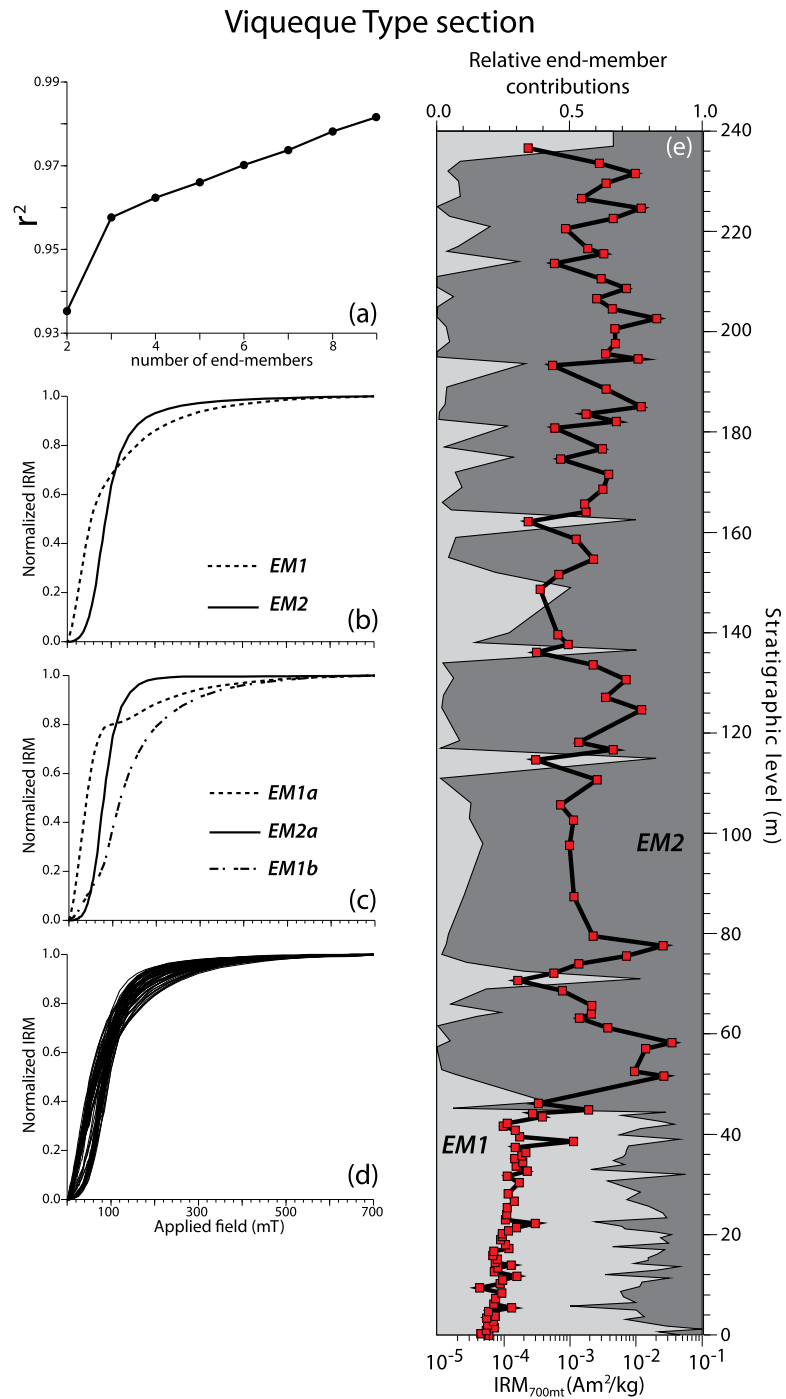
Figure 3. The end-member model results of the Viqueque Type section. (a) Coefficient of determination versus the number of end-members. There is a clear break-in-slope at the three end-member model. (b and c) The IRM acquisition curves of the end-members for the two and three end-member model. The curves with approximately the same shape have identical labels (e.g., *EM1* and *EM1a*). (d) The input IRM-acquisition curves of all the even-numbered sample levels (for visual appreciation and clarity the odd-numbered levels were omitted). (e) The relative contributions of the end-members to each sample level for the two end-member model. The black line indicates the IRM_{700mT} intensity (logarithmic scale).

"splits" into the two other end-member curves (*EM1a* and *EM1b*) of the three end-member model. Because the rock magnetic results (see below) do not show sufficient difference between *EM1a* and *EM1b* and the interpretation of the magnetic mineral suites would become needlessly complicated for the present purpose, the two end-member model is preferred for its comparative simplicity and straightforwardness. The

Figure 4. The end-member model results of the Cailaco River section. (a) Coefficient of determination versus the number of end-members. The break-in-slope is at three end-members, although this break is distinctly less pronounced compared to the Viqueque Type section. (b and c) The IRM end-member curves of the two and three end-member model. Dotted/continuous lines reflect the similarities with end-member curves of the Viqueque Type section. (d) The input IRM-acquisition curves of all the even-numbered sample levels (see caption to Figure 3 for the omission of odd-numbered levels). (e) The relative contributions for the two end-member model. The white intervals are unexposed. Note the high EM2 contribution interval between 260 and 380 m. The black line indicates the IRM$_{700mT}$ intensity (logarithmic scale).

coefficient of determination is 0.935 and 0.955 for the Viqueque Type section for the two and three end-member solutions, respectively; lower values are obtained for the Cailaco River section, respectively, 0.81 and 0.84. These values are well above the threshold of ∼0.7, considering the number of datapoints (61). For a more detailed discussion on the optimal end-member model, see supporting information B.

In the two end-member solutions of both sections, **EM1** consists of 60% of a soft component with a coercivity range between 0 and 50 mT while the remaining 40% is represented by a broad coercivity fraction ranging up to ~500 mT for the Viqueque Type section and up to 700 mT for the Cailaco River section. In both sections, **EM2** consists of a single sigmoidal shaped curve with the largest increase in IRM between 30 and 120 mT. Below 30 mT and above 120 mT almost no increase is observed. **EM2** can be considered saturated at 700 mT in both sections, while **EM1** is nearing saturation in the Viqueque Type section and slightly less so in the Cailaco River section. For the Viqueque Type section, the relative contributions of the end-members to the individual IRM-acquisition curves of each sample level (Figure 3e) illustrate the lithological transition at ~40 m from the base. In the limestones and pelagic marls, **EM1** is the dominant end-member, **EM2** is dominant in the shale interval except for irregularly spaced levels at which **EM1** has a larger contribution. In the Cailaco River section (Figure 4e), the relation between lithology and end-members is less apparent: in the lower 260 m of section **EM1** makes up 60–95% while it is 50–60% in the topmost 70 m (430–500 m stratigraphic level).

In the Viqueque Type section, the IRM$_{700mT}$ (Figure 3e) also relates to the end-member allocation and lithology. In general, the IRM$_{700mT}$ is an order of magnitude less in the limestone and marl samples from the bottom of the section ($10^{-5}-10^{-4}$ Am^2/kg) than in the shale sample levels ($10^{-3}-10^{-2}$ Am^2/kg) higher up in the stratigraphy. Note that the shale sample levels with a large **EM1** contribution have a significantly lower IRM$_{700mT}$ than the other shale sample levels. Some anomalously high peaks in IRM$_{700mT}$ are observed in the interval between 50 and 60 m, these intensities are an order of magnitude higher (5×10^{-2} Am^2/kg) than average **EM2**-dominated samples and are not isolated into a separate end-member when using a higher number of end-members. In the Cailaco River section most samples are dominated by **EM1** with the concomitant low IRM$_{700mT}$ values ($10^{-5}-10^{-4}$ Am^2/kg, Figure 4e). Except for a few incidental samples scattered throughout the section with high **EM2** contributions, **EM2**-dominated samples with their high IRM$_{700mT}$ values ($\sim 3 \times 10^{-3}$ Am^2/kg) are essentially confined to the 260–380 m stratigraphic interval.
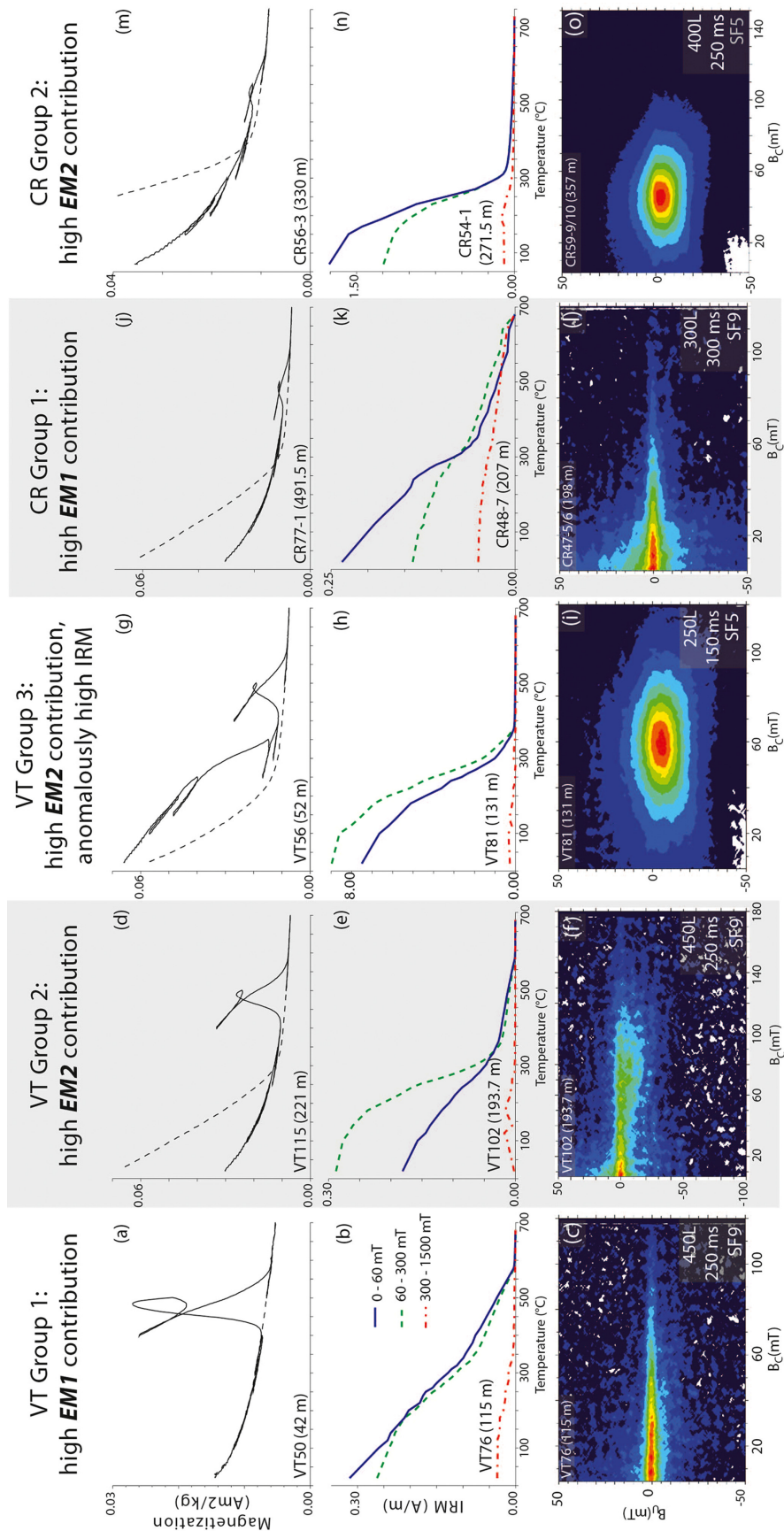
5.2. Rock Magnetic Results

The rock magnetic results—thermomagnetic runs, thermal demagnetization of three-axis IRM, and FORC-analysis—enable the distinction of groups of sample levels with similar rock magnetic properties. Three of these groups are recognized in the Viqueque Type section and two in the Cailaco River section (Figure 5). The sample levels in the first and second group of both sections match with high contributions of **EM1** and **EM2,** respectively. The third, much smaller, group of sample levels in the Viqueque Type section matches with high **EM2** contributions as well. Here we briefly describe the main results of the five groups; a more in-depth description is provided in supporting information B.
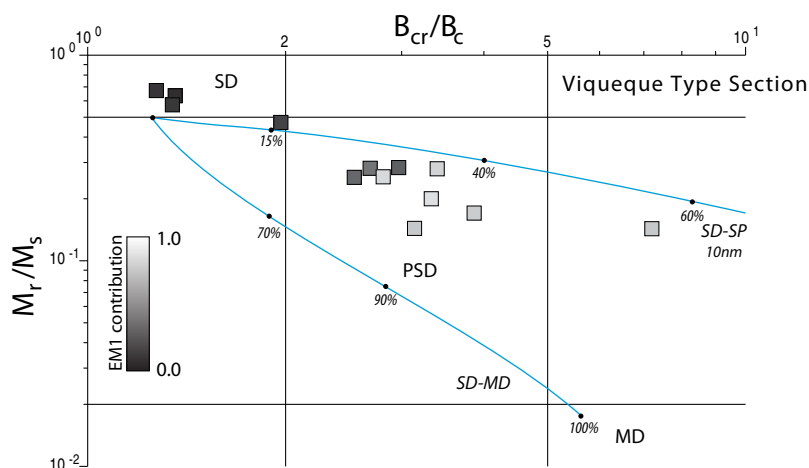
5.2.1. Viqueque Type Section

The first group of samples (Figures 5a–5c) is dominated by **EM1**. The high field thermomagnetic behavior of this group up to 400°C is characterized by dominantly paramagnetic particles (Figure 5a) without irreversible behavior. The thermal properties above 400°C are constrained by the thermal demagnetization of the composite three-axis IRM. The dominant magnetic component recognized in these runs (Figure 5b) has a maximum unblocking temperature of 580°C, coinciding with the Curie temperature of magnetite. A smaller, second component is recognized as a steeper decrease in remanence between 150 and 300°C possibly pointing toward greigite. The FORC-diagrams (example in Figure 5c) show somewhat varying results: generally, horizontal contours with almost no vertical spread are observed, indicating marginal magnetic interaction. The horizontal spread along the B$_u$ = 0 axis centered close to the origin implies a grain size distribution with a considerable portion of particles with relaxation times just above strictly SP relaxation times.

The second group in the Viqueque Type section (Figures 5d–5f) is dominated by **EM2** and shows a concave decreasing thermomagnetic curve (Figure 5d). These curves typically show reversible behavior up to 250°C, after which some irreversible behavior is noticed. These points toward greigite, supported by the demagnetization runs of the three-axial composite IRM showing a prominent decay up to 350°C (Figure 5e). A much smaller contribution of magnetite with a maximum unblocking temperature of 580°C is observed as well. The FORC-diagrams of this group (Figure 5f) shows the same component on the B$_u$ = 0 axis centered close to the origin, related to magnetite. A prominent second component is recognized in the FORC diagram, characterized by closed concentric contours with significant vertical spread around a central peak

Figure 5. Typical rock magnetic results recognized in the (a–i) Viqueque Type (VT) section (divided in three groups) and the (j–o) Cailaco River (CR) section (two groups). For each group, a representative thermomagnetic run (dashed line is the major cooling loop), a representative demagnetization diagram of a composite three-axis IRM, and a typical FORC-diagram is shown. For the FORC-diagrams: B_b (range over which FORCs are measured) = ± 500 mT, saturation field = 1.5–2 T, L = number of measured FORCs, ms = averaging time used in milliseconds, SF = smoothing factor used for the calculation of the FORC representation by an inhouse developed algorithm using truncation of the diagram near the B_C = 0 axis.

Figure 6. Day plot showing the hysteresis parameters of 13 samples of the Viqueque Type section. The samples cover the whole range of end-member contributions that is observed in the Viqueque Type section. The gray-value scale bar indicates the relative end-member contributions. SD, PSD, and MD fields for magnetite as well as theoretical mixing curves by *Dunlop* [2002] are included for reference. However, some caution is appropriate here, as the lines and fields on the Day plot are based on magnetite and might not be representative for mixing of other magnetic minerals. Nonetheless, a mixing trend between SD greigite and quasi-SP magnetite can be recognized.

relatively high up the B_c-axis: 50–75 mT. This FORC-signature indicates interacting single domain (SD) particles, most likely this signature represents the greigite.

The third, much smaller group in the Viqueque Type section (Figures 5g–5i) is dominated by **EM2** as well and only encompasses the sample levels with anomalously high IRM_{700mT}. This is reflected in the thermomagnetic runs (Figure 5g); a very high initial magnetization is followed by a relatively steep irreversible decrease in magnetization between 200 and 350°C, indicating a large amount of greigite. This is supported by the thermal demagnetization behavior of the three axial composite IRM, showing that only greigite is present (Figure 5h). The FORC-diagrams of these samples show one very clear component (Figure 5i): the concentric contours related to greigite. Magnetite is not observed in the rock magnetic properties.

Sample levels that are not dominated by a single end-member, but contain a mixture of **EM1** and **EM2**, show rock magnetic properties that are a mixture between typical properties of group 1 and 2. This is nicely visualized in a Day-plot of M_r/M_s versus B_{cr}/B_c [*Day et al.*, 1977] (Figure 6) for a selection of samples from the Viqueque Type section with varying end-member contributions. Samples with a high **EM2**-contribution plot in the SD-field (the field division and mixing lines in the Day-plot are based on magnetite). **EM1**-dominated samples plot in the top-right part of the PSD-field, also even beyond the $B_{cr}/B_c = 5$ line. The SD-SP mixing envelope expresses the mixing trend. The calculated trend of 10 nm particles [*Dunlop*, 2002] is shown; for the mixing percentages relevant here the size of the SP particles is less critical. The fairly low M_r/M_s values could point to the influence of nonuniaxial particles; *Dunlop*'s [2002] calculations are based on uniaxial particles.

5.2.2. Cailaco River Section
The first group, associated to **EM1**, shows rock magnetic properties (Figures 5j–5l) that are essentially the same as group 1 of the Viqueque Type section (Figures 5a–5c). Only the thermal demagnetization of a composite three-axis IRM is subtly different (Figure 5k): the hard and intermediate coercivity components unblock up to 680°C indicating hematite.

The second Cailaco River group, associated with high **EM2** contributions, also shows rock magnetic properties (Figures 5m–5o) that are largely similar to group 2 of the Viqueque Type section (Figures 5d–5f). The greigite-related properties are expressed more strongly, indicating a higher content of greigite in the sample levels. The FORC density maximum lies at a coercivity of ~45 mT (Figure 5o), distinctly lower than that of the **EM2**-dominated samples in the Viqueque Type section. This is in one of the observations supporting a smaller greigite particle size for the Cailaco River section.

Mixed properties of the Cailaco River section groups described above are not observed, unlike in the Viqueque Type section. This indicates a "binary" division of sample levels: they are either dominated by a magnetite-hematite magnetic mineralogy or have a higher intensity greigite mineralogy with high IRM_{700mT} values.
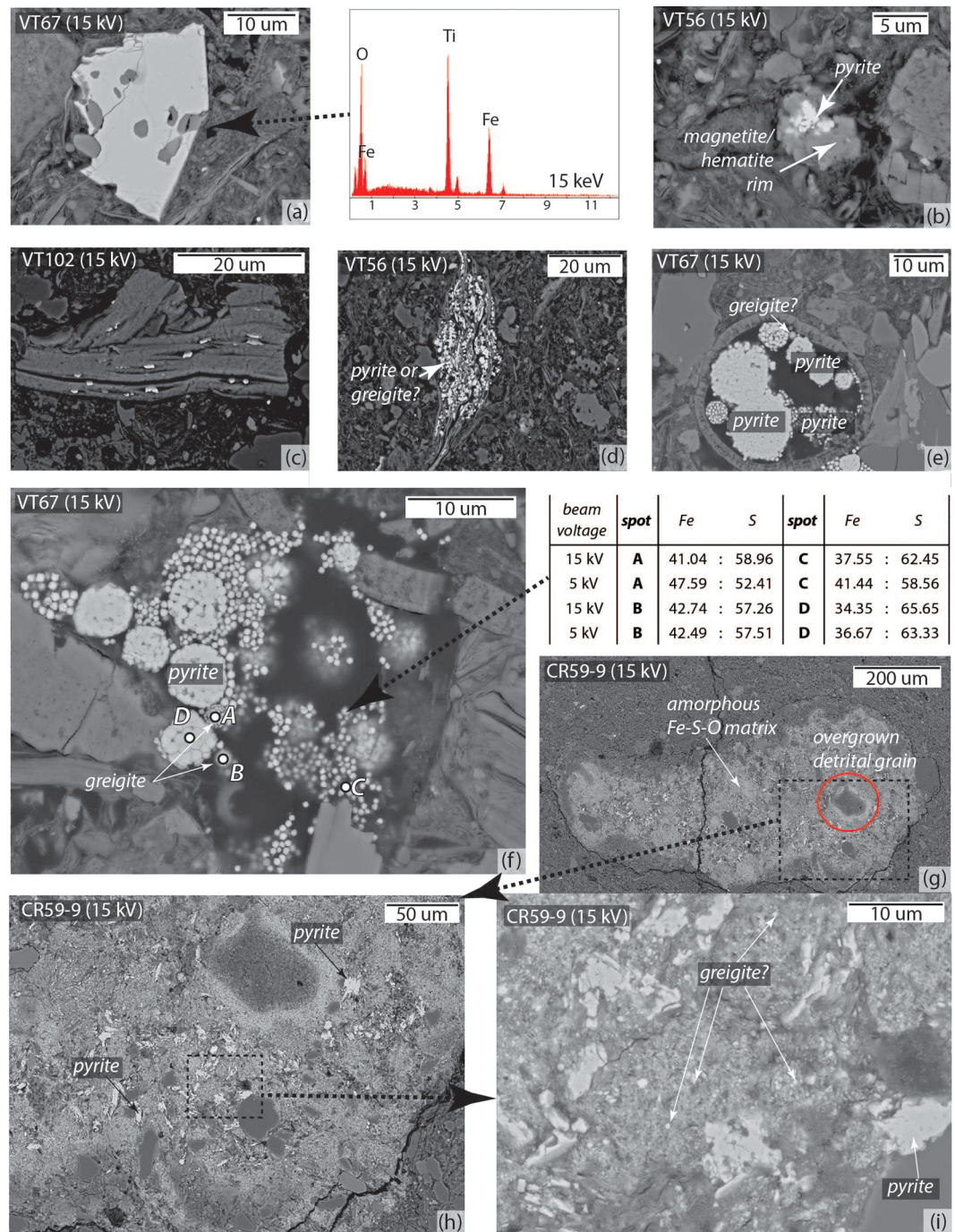
Figure 7. Results of the SEM and EDS analysis, for each picture, the voltage of the electron beam is given. (a) Through (f) Viqueque Type (VT) section, (g) through (i) Cailaco River (CR) section. (a) Detrital bright grain, showing some dissolution features, identified as ilmenite (EDS-spectrum included). (b) Some oxidation products around a pyrite grain recognized as magnetite or possibly hematite. (c) Typical sheet silicate with some incidental iron-sulfide grains grown in between the sheets. (d) Massive intergrowth of iron sulfides at a large sheet silicate mineral, only observed in the anomalously high intensity sample level VT56. (e) Typical cluster of framboids associated with normal intensity *EM2* sample levels. The larger framboids are identified as pyrite, the tiny framboids in between are most likely greigite, although often too small for reliable EDS-analysis. (f) Framboid cluster in which greigite is reliably identified. Spots A and B yield typical greigite ratios (table on the right) for a 15 and 5 kV electron beam. Spot C is too small for reliable identification of the iron sulfide grains, spot D shows clear pyrite ratios. (g) SEM-picture of a nodule that is typical for the EM2-dominated sample levels. Note the relatively large size. An overgrown detrital quartz grain is indicated by the circle. (h) Zoom of the nodule, showing large overgrown pyrite crystals. (i) Close-up of some pyrite crystals "floating" in the amorphous matrix of iron sulfides. Some small round grains can be recognized in the matrix, these might be greigite grains.

5.3. Optical Microscopy and SEM Observations

Four "habitats" or modes of occurrence for magnetic minerals are revealed by the optical microscopy study. The first three occur in both sections while the 4th is unique to the Cailaco River section. SEM and EDS-analysis extends the optical microscopy; particular attention is paid to the fine-grained iron sulfide phases, which comprise a typical greigite mode of occurrence [e.g., *Roberts and Weaver*, 2005; *Hüsing et al.*, 2009].

Habitat 1: bright detrital grains which look like (titano-)magnetite or ilmenite, present in both sections and in all samples regardless of lithology. Most of these grains show dissolution features and holes. According to EDS-analysis, they appear to be predominantly ilmenite for all samples analyzed (Figure 7a). This habitat can be discarded as potential magnetic carrier. Magnetite and hematite are very incidentally observed as oxidation rims around pyrite grains (Figure 7b), but are negligible in volume.

Habitat 2: iron sulfide grains grown in between detrital sheet silicate grains, present in both sections. This morphology is recognized in low abundances in marl and shale samples, except for thin sections VT56 in which massive intergrowths with large sheet silicates are observed. The iron sulfides between the sheet silicates are in general too small for reliable EDS-analysis. In most thin sections, only a few grains are observed between the sheets (Figure 7c), except for sample VT56 (Figure 7d). Iron sulfides residing between sheet silicates volumetrically dominate this particular sample, in which the presence of greigite is very plausible. However, the identification of greigite or pyrite cannot be faithfully established by EDS-analysis due to interference of the surrounding sheet silicate material.

Habitat 3: iron sulfide framboids and clusters of framboids, the latter are more abundant in the *EM2*-rich samples. In the Cailaco River section, the framboids are slightly smaller and less abundant than in the Viqueque Type section. All the individual large framboid particles are identified as pyrite in both sections. In the Viqueque Type section, the framboid clusters contain also very fine grained small framboids in between the larger pyrite framboids (Figures 7e and 7f). Their Fe:S-ratios (EDS-analyses) strongly hint at greigite (Figure 7f, spots A, B, and C; compare the 15 kV with the 5 kV analysis of these spots). The ratios significantly differ from the pyrite ratios obtained for the large framboids (Figure 7f, spot D). Reliable measurements could not be performed on the tiny individual iron sulfide grains located between these framboids, but it is likely that they are greigite grains as well due to their similar grain size and morphology. This very fine grained greigite phase is not recognized in each thin section, solely in the *EM2*-dominated thin sections of the Viqueque Type section. In the samples from the Cailaco River section only pyrite framboids were observed, the small greigite framboids do not seem to be present.

Habitat 4: this habitat is unique for the Cailaco River section and is found in *EM2*-dominated samples between 260 and 380 m stratigraphic level. It appears as large patches or nodules (up to 1–2 mm) of a hard phase with medium brightness under the optical microscope. Under the SEM they consist of a bright, fine-grained amorphous matrix (Figures 7g and 7h). Remains of larger pyrite grains are identified within the matrix. These grains are overgrown and partially dissolved but might have had a euhedral shape before being overgrown. Detrital (quartz) grains are overgrown as well, but are not chemically affected by the matrix. In higher resolution, the matrix consists of small iron sulfide grains and an amorphous ground mass (Figure 7i). The iron sulfide grains are unfortunately too small to be analyzed individually. The matrix and grains together give an EDS-spectrum showing large peaks of oxygen, sulfur, and iron, and smaller peaks of aluminium, silicium, and calcium. It is very plausible that the greigite resides within this chaotic amorphous matrix, especially since the other possible habitats are present only in minor volumes or not present at all in these thin sections.

5.4. Interpretation of the End-Members

The interpretation of the two end-members is nearly identical for the two sections: *EM1* represents magnetite with a considerable portion of quasi-SP particles. In the Viqueque Type section, there is no hematite contribution to *EM1* while in the Cailaco River section a small hematite contribution to *EM1* is detected. *EM2* in both sections shows a very dominant interacting SD greigite population (no pyrrhotite, see arguments in supporting information C1). Here we interpret the end-members in terms of remanence acquisition.

The magnetite of *EM1* is incidentally observed during microscopic research as the oxidation product of pyrite. Likely, the quasi-SP magnetite grains are too small to be observed in situ by the SEM. Besides

oxidation, partial dissolution during burial of detrital magnetite particles is responsible for the broad coercivity range (this can be supported by the magnetite-related central ridge along the $B_u = 0$ axis in the FORC diagrams; see supporting information C1 for a detailed discussion). The magnetite (and hematite) suite is therefore interpreted to be of mainly detrital origin and to carry a significant VRM component. A stable DRM (Detrital Remanent Magnetization) is less likely to reside in **EM1**-dominated samples.

The greigite mineral suite (**EM2)** in the Viqueque Type section is pristine; the greigite grains are visually not degraded. This is supported by the rock magnetic properties, which show dominant SD behavior. The mineral suite has an in situ, diagenetic origin: within pyrite-dominated framboid clusters, containing multiple generations of iron-sulfide growth, the greigite is recognized as very fine individual grains or as tiny framboids. This morphology of greigite is commonly observed elsewhere [*Jiang et al.*, 2001; *Roberts et al.*, 2005; *Hüsing et al.*, 2009; *Rowan et al.*, 2009] and relates to early diagenetic processes [*Berner*, 1984; *Kao et al.*, 2004; *Fu et al.*, 2008; *Rowan et al.*, 2009]. Greigite framboids consist of a large number of small grains packed closely together, explaining the high interaction observed in the FORC-diagrams. As argued before: "early" diagenetic is relative and the timing of the CRM acquisition can vary from 1 to 100 kyr after deposition [*Rowan et al.*, 2009], depending on sedimentation rates. To establish the timing of acquisition as precise as possible, the paleomagnetic signals must be analyzed and compared to other, primarily biostratigraphic, age constraints.

Besides the frequently occurring magnetite and framboidal greigite suites in the Viqueque Type section, a second greigite suite is recognized in this section as well: iron sulfide intergrowths in large sheet silicates typified by sample VT56. This particular sample has the highest IRM_{700mT} of all samples and does not show many framboidal pyrite clusters. Therefore, it is expected that the greigite resides within these frequently occurring massive intergrowths. The large number of closely packed greigite grains causes the large interaction as determined in the FORC-diagrams. This greigite suite is of a late diagenetic origin [*Canfield et al.*, 1992; *Jiang et al.*, 2001; *Roberts and Weaver*, 2005]. It can be argued whether all SD greigite related to **EM2** resides either in the early diagenetic framboids or in the late diagenetic sheet silicates. The first seems more likely as the framboidal morphology is observed in *all* thin sections and the voluminous intergrowths merely in one thin section. This sheet silicate intergrown greigite is a sporadically occurring population on top of the framboidal greigite, causing high NRM and IRM intensities at some specific sample levels. This is supported by the IRM_{700mT} data in which a few anomalously high peaks are observed.

A comparatively straightforward model of the sedimentary genesis can explain the simultaneous presence of the early diagenetic greigite and the detrital magnetite in the Viqueque Type section, in which the magnetite is subject to reductive dissolution during burial and the greigite is formed during the pyritization process, resulting in mixtures of the two (illustrated by the Day-plot in Figure 6). The observed variations can be related to changing sedimentation rates. This conceptual genesis model is explained in detail in supporting information C2.

In the Cailaco River section, the greigite suite has another origin than its Viqueque Type section counterpart, although this difference is established clearest by microscopic observations. The morphology of the nodules rules out a biogenic or early diagenetic origin. The nodules are confined to an interval between 260 and 380 m from the base of the section. The large oxygen peak measured in the matrix might result from oxidation of metastable iron sulfide phases, resulting in some overgrowth of detrital grains. The nodules seem to be part of the sediment since deposition, no in situ growth-related features are recognized in the surrounding sediment. The amorphous matrix within the nodules makes it nearly impossible to postulate a reliable late diagenetic conceptual model. A very similar chaotic nodular morphology is also described by *Giovanoli* [1979], but as he was one of the first authors to recognize greigite he did not propose a clear formation process. The absence of framboids, in contrast with other greigite-bearing nodules described in literature [e.g., *Van Dongen et al.*, 2007], hints at a late diagenetic origin of the greigite residing in this specific interval. Thus, it is unsuited for magnetostratigraphic purposes.

6. Paleomagnetic Interpretation

First, we concentrate on the Viqueque Type section for which we show that a polarity sequence can be retrieved. In the second subsection, we will discuss the Cailaco River section because—while being unsuited for magnetostratigraphy—it shows a distinct tectonic rotation.
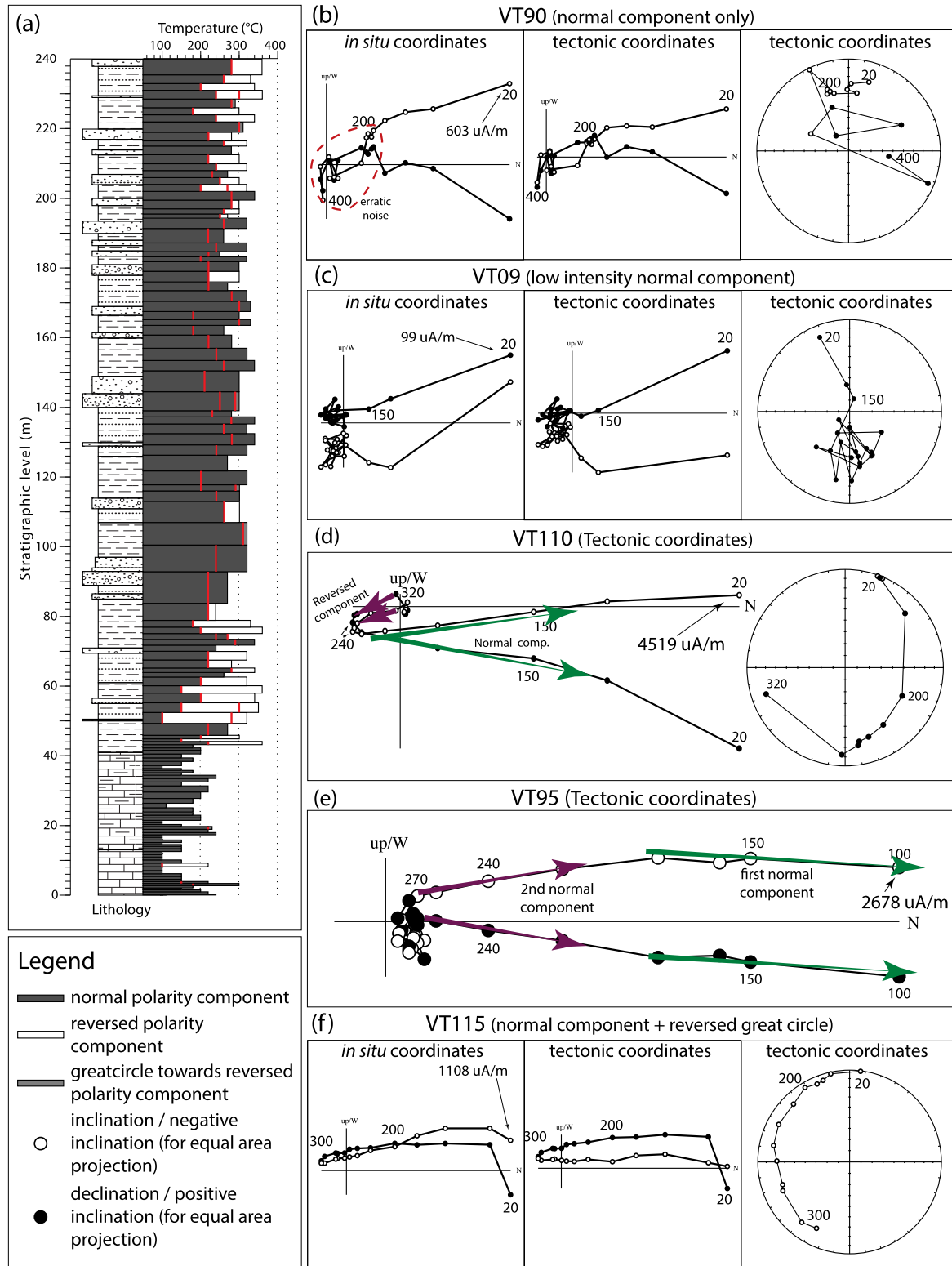
Figure 8. (a) The polarities of the NRM-components versus the temperature of all sample levels of the Viqueque Type (VT) section, gray lines separate the different components. The lithological column is given for reference. (b and c) Examples of samples with solely one polarity component, Figure 8b is a shale sample level, Figure 8c is a pelagic limestone sample level that is fully demagnetized at 150°C. Higher-temperature datapoints are influenced by the (small) residual field in the SQUID magnetometer. (d) Typical example of a Zijderveld diagram showing a normal low-temperature component and a high-temperature reversed component. (e) Typical example of two different normal components. (f) Clear example of a great circle toward a reversed polarity direction at higher temperature. Note that Timor Leste is located on the southern hemisphere; i.e., normal polarity has upward directed inclinations.
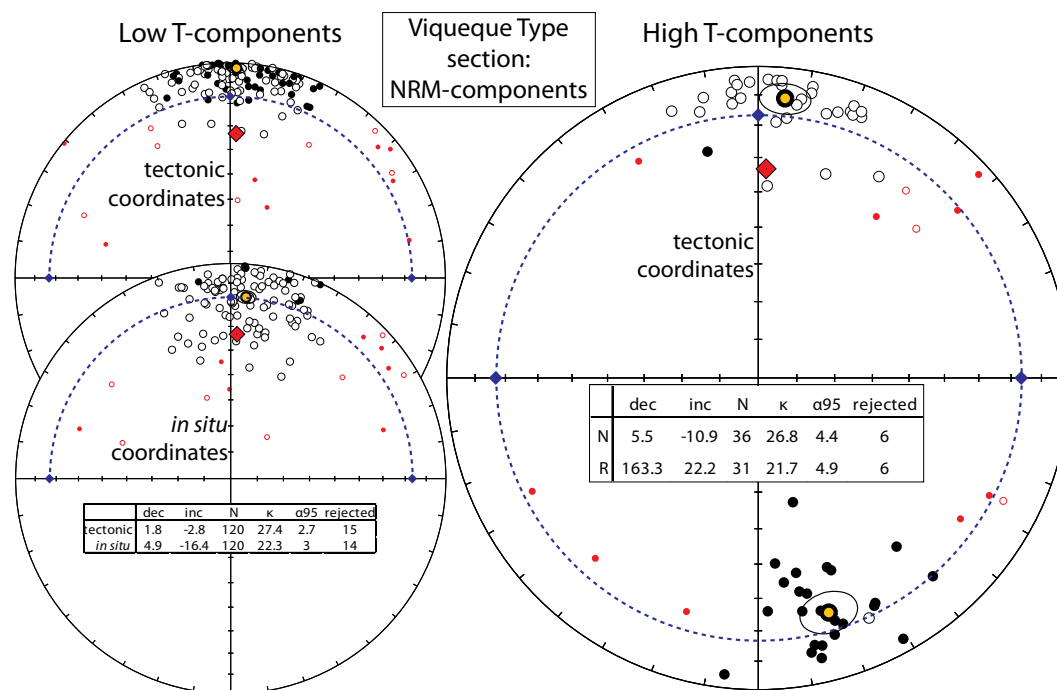
Figure 9. Viqueque Type section. Equal area projections of the (left) low-temperature and (right) high-temperature NRM-components. Open (closed) symbols indicate negative (positive) inclinations. Gray symbols are directions rejected by the variable angle cutoff [*Vandamme*, 1994]. The dashed line indicates the GAD-declination (I = −17°), the large diamond is the present-day magnetic field in Timor. Mean directions are indicated by the larger gray symbols and quantified in the tables. Dec = declination, inc = inclination, N = number of components, κ = Fisher precision parameter (Fisher 1953), α95 = 95% cone of confidence, rejected = number of rejected samples by the Vandamme cutoff.
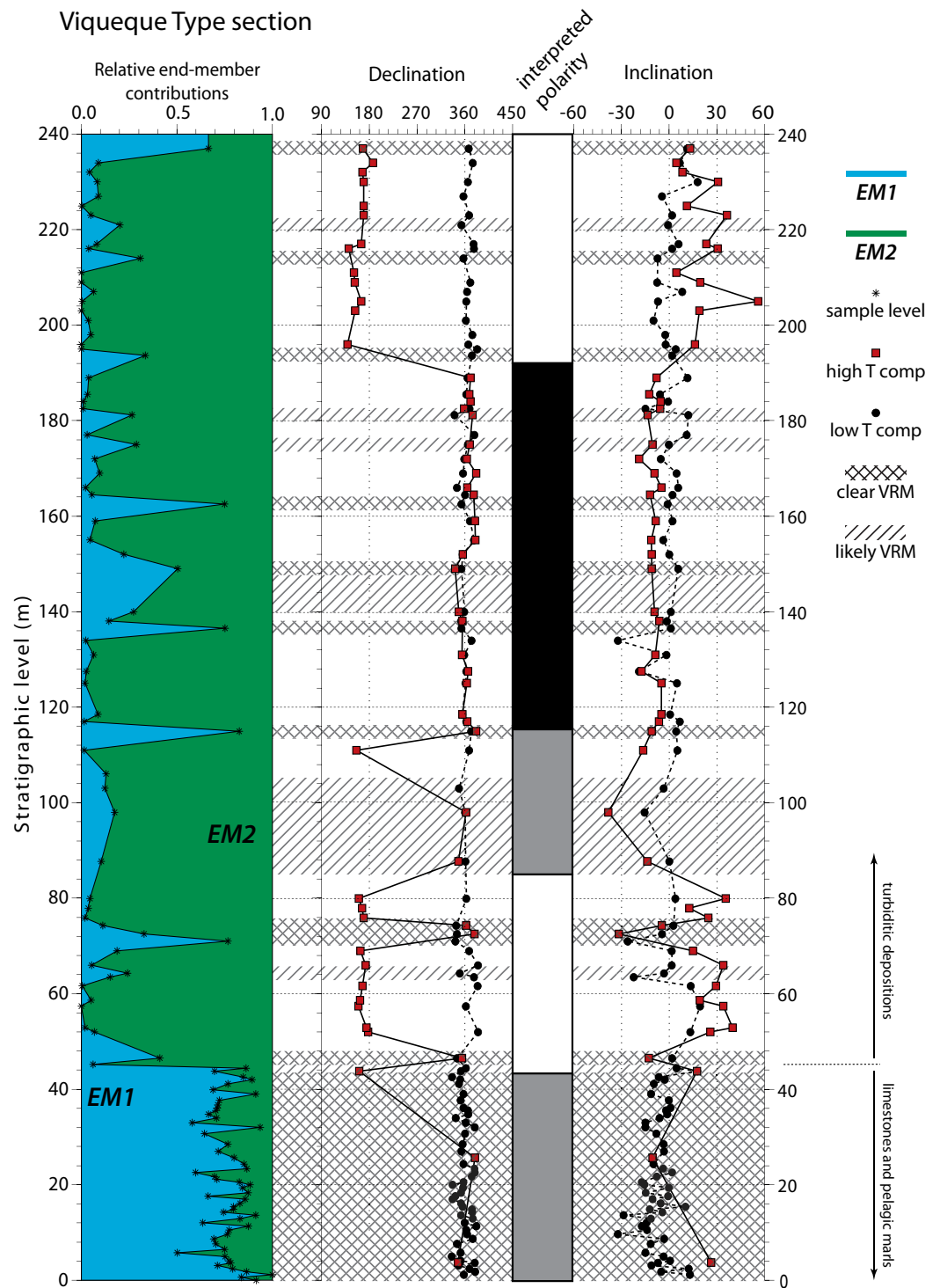
6.1. Viqueque Type Section

6.1.1. NRM-Components

The magnetite-dominated samples levels yield very low NRM-intensities that are reduced quickly to instrumental noise level. Due to a small offset by a residual field in the SQUID-magnetometer, which is not fully compensated by the software, the danger exists of interpreting great circle traces that are instrument related. Therefore, a conservative approach toward great circle traces is taken here. All NRM polarity components recognized at 50°C and higher in the thermal demagnetization diagrams are logged systematically and are presented in Figure 8a (see supporting information D1 for a full table with components).

The observed NRM components (Figure 8a) can be divided into two populations: (1) a low-temperature component up to 200°C, occasionally extending up to 280°C, which *always* has a normal polarity and is recognized in all sample levels (Figures 8b and 8c). (2) A high-temperature component, typically recognized from 200 to 240°C onward, with either a reversed (Figure 8d) or normal (Figure 8e) polarity direction or a conclusive great circle trace (Figure 8f). These high-temperature components are exclusively observed in the shale-turbidite interval (Figure 8a). Those shale samples that do not contain this high-temperature component show a lower absolute NRM-intensity and decay to noise level at lower temperatures. The low-temperature normal component and the high-temperature normal component do not share a ctmd (common true mean direction) and are therefore statistically significantly different. With the variable cutoff angle approach [*Vandamme*, 1994], outliers are filtered out and the mean directions are obtained for the two populations (Figure 9).

For population 1 (the low-temperature components), the mean inclination in in situ coordinates (Figure 9a) coincides with the GAD (Geocentric Axial Dipole) inclination (I = −17°, blue dashed line in Figure 9) of the present-day position of Timor. This NRM component thus postdates the tilting of the sediments and is therefore regarded as a secondary component, presumably of viscous origin. It resides in a mineral suite present in all lithologies as the (VRM) component is essentially the same regardless of lithology. We therefore link this component to the magnetite suite, for which a quasi-SP behavior expressed as a VRM is anticipated.

Figure 10. The NRM component quality label index and the resulting polarity pattern for the Viqueque Type section. (first column) Relative contributions of the two end-member model (see Figure 3). (second column) Declinations of the low-temperature (black circles) and high-temperature (red squares) components plotted versus stratigraphic level. (third column) Final interpretation of the polarity pattern, gray color indicates the unknown polarity intervals. (fourth column) Inclination versus the stratigraphic level, symbols are equal to the declination data. The shades indicate the three quality label classes: no shade for class 1 (reliable), cross hatching for class 2 (unreliable), and hatching for class 3 (likely to be unreliable).

After tilt correction, the high-temperature normal and reversed polarity components of the second population differ from the GAD by $I = -6°$ and $I = +6°$, respectively (Figure 9b). In in situ coordinates the mismatch with the GAD becomes much larger, making a posttilt origin unlikely. Its dual-polarity indicates a geologically stable remanence signal and the components are completely demagnetized at 300–360°C. We therefore infer that this ChRM component resides in the SD early diagenetic greigite suite. Supporting information D2 provides some extra discussion on the paleomagnetic data of these higher-temperature components.

The anomalously high IRM_{700mT} sample levels associated with massive intergrowth of greigite yield anomalously high NRM intensities as well. The polarity residing in these samples is equal to the high temperature polarities of the adjacent samples; only the normal viscous overprints at lower temperatures are more obscured. It thus seems that these incidental levels do not interfere with the general polarity pattern and are therefore deemed trustworthy.

6.1.2. Constructing the Polarity Pattern

Fifty-five reliable ChRM (high temperature) directions (30 normal, 25 reversed) are used to construct the magnetostratigraphic framework of the Viqueque Type section (Figure 10). The viscous low-temperature directions are plotted for completeness. A consistent polarity pattern is obtained from the high-temperature ChRM directions. Starting at the base of the section a few scattered normal polarity samples occur, followed by a dominantly reversed interval from 44 to 115 m intervened by short normal polarity intervals. Between 115 and 190 m a normal polarity zone is recognized, followed by a reversed polarity interval up to the top of the section.

By comparing the observed NRM components to the contributions of the magnetic mineral suites from the end-member modeling, we can assess the reliability of the ChRM components. To do so, three qualitative quality label classes are assigned to the ChRMs (shaded areas in Figure 10). This is based on the end-member contributions and the demagnetization behavior (e.g., intensity, noise level). Quality 1 (no hatching in Figure 10): reliable levels dominated by greigite showing clear demagnetization behavior and high NRM intensities. Quality 2 (cross hatching): clear VRM, therefore unreliable. This includes all **EM1**-dominated sample levels, regardless of the demagnetization behavior. These sample levels are discarded for the construction of the final polarity pattern. Quality 3 (diagonal hatching): likely to hold a VRM, based on the observed demagnetization behavior in accordance with the end-member contributions. These sample levels are not very reliable and the ChRM's polarity must be supported by the polarities of adjacent reliable sample levels not to be discarded.

Revising the polarity pattern using these quality indexes yields a surprisingly simple magnetic polarity pattern (Figure 10, third column). It consists of an interval of unknown polarity (gray color) for the limestones and marls at the base of the section, followed by a reversed polarity interval from the lithological boundary up to 85 m and subsequently by an uncertain polarity interval up to 115 m stratigraphic level. This uncertain polarity interval is defined by a very low number of reliable ChRMs, which is partly caused by some thick turbidite deposits and relatively wide sample spacing. The samples that are present within this interval yield conflicting polarities. The interval above 115 m is undisputed and consists of a normal polarity interval up to 190 m, followed by a reversed interval up to the top of the section.

6.1.3. Correlation to the GPTS

Although a reliable polarity pattern is obtained, it is still based on an early diagenetic CRM. An independent age constraint is needed to further evaluate the timing of the CRM acquisition for an integrated stratigraphic frame. Therefore, we apply the biostratigraphy of *Tate et al.* [2014] and *Haig and McCartain* [2007] to correlate the polarity record of the Viqueque Type section to the Geomagnetic Polarity Time Scale (GPTS) of the Neogene period [*Hilgen et al.*, 2012].

The resulting correlation is straightforward (Figure 11): due to two hiati, dated in the basal part of the section [Tate et al., 2014], the first reversed polarity interval (between 43 and 85 m) cannot be older than the Mammoth subchron (C2An.2r) within the Gauss Chron. This correlation is supported by the first occurrence (FO) of *Globorotalia tosaensis* recorded by *Haig and McCartain* [2007] at 45 m and by *Tate et al.* [2014] at 27 m. This bioevent is dated at 3.35 Ma [*Wade et al.*, 2011]. The normal polarity interval between 115 and 192 m is correlated to C2An.2n. The position of the polarity reversal between these two subchrons in this section cannot be pinpointed more accurately than somewhere in between 85 and 115 m stratigraphic
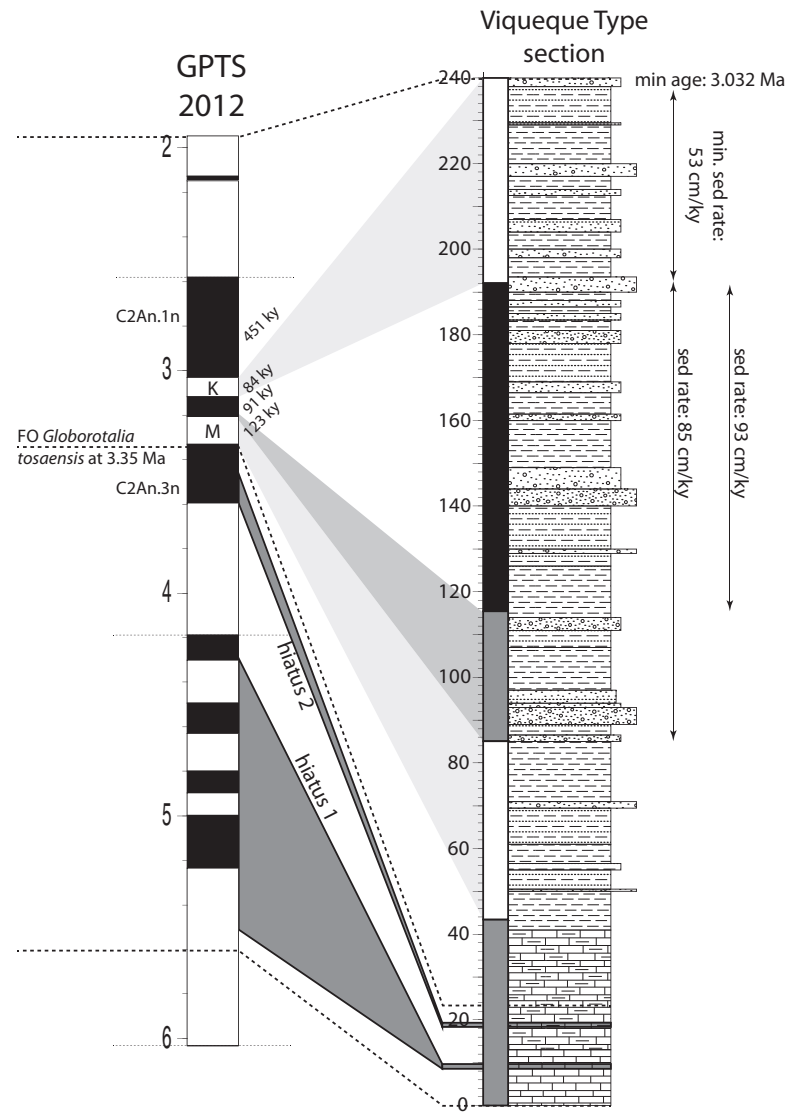
Figure 11. The correlation of the polarity record of the Viqueque Type section to the geomagnetic polarity time scale (GPTS) with the help of biostratigraphically constrained hiatuses and first occurrence (FO) of *Globorotalia tosaensis* [Tate et al., 2014]. K = Kaena subchron, M = Mammoth subchron, and sed rate = calculated sedimentation rates based on this polarity correlation.

level. The reversed polarity interval from 192 m at the top of the section correlates to the Kaena subchron (C2An.1r). The base of the Kaena is dated at 3.116 Ma [*Hilgen et al.*, 2012].

The minimum and maximum sedimentation rates of 85 and 93 cm/kyr for the normal polarity interval can be calculated by in or excluding the unknown polarity interval between 85 and 115 m. Extrapolating these rates yields ages of 3.063 or 3.068 Ma for the top of the section. Since C2An.1n is not reached (no normal polarity at the top of the Viqueque Type section), the youngest possible age for the top of the section would equal the top of the Kaena subchron at 3.032 Ma. The base of the interval that we correlate to the Mammoth subchron, unfortunately, cannot be constrained by further extrapolation of the sedimentation rates as the lithological boundary between shales and pelagic marls very likely indicates a transition in sedimentation rate.

6.2. Cailaco River Section

The greigite in the Cailaco River section is late diagenetic. So, the ChRM cannot be used for magnetostratigraphic purposes. Nonetheless, we examine the thermal demagnetization data here to test the
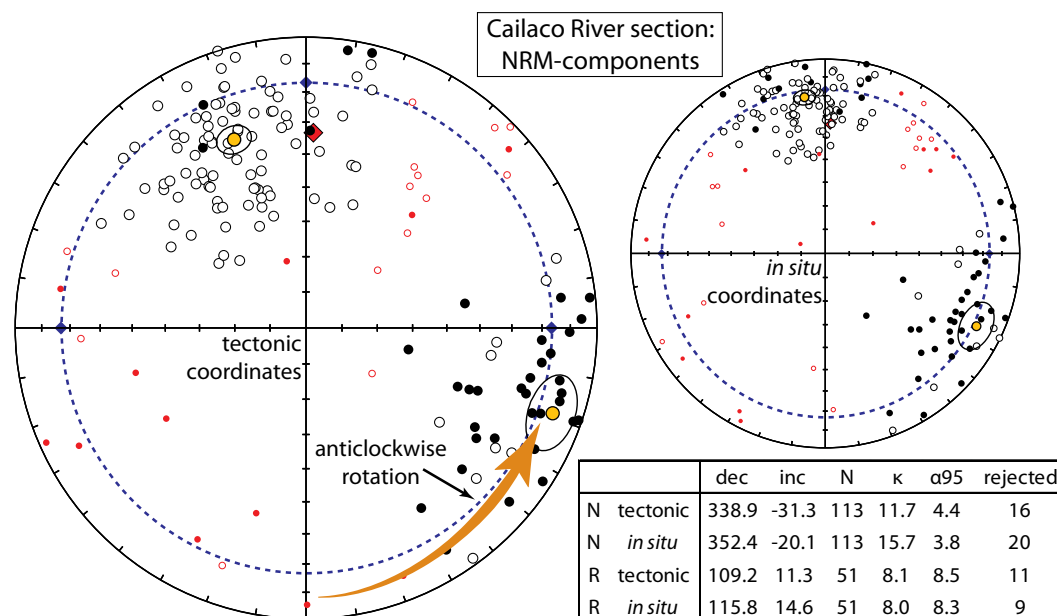
Figure 12. Cailaco River section. Equal area projections of (left) NRM-directions in tectonic and (right) in situ coordinates. Open (closed) symbols indicate negative (positive) inclinations. Gray datapoints are rejected directions by the variable angle cutoff [*Vandamme*, 1994], the dashed line is the GAD-inclination (I = −17°) of the current latitude of Timor. Mean directions of the two populations are indicated by the larger gray symbols in the projections and are summarized in the table (for key see Figure 9). Note the large anticlockwise rotation of the reversed polarity population.

interpretation of the IRM acquisition end-member model. The demagnetization diagrams are characterized by low intensities (<1000 μA/m) except for the greigite-rich samples. Well-defined low-temperature and high-temperature components are not recognized and the strictly binary subdivision of greigite-dominated and magnetite-dominated samples is more apparent (see supporting information E for a full table with components). The magnetite-rich samples typically show a normal polarity component up to 250°C that behaves as a typical VRM overprint (perfectly North declination and inclination equal to the GAD in in situ coordinates, Figure 12). Only incidentally, a possibly reversed polarity component is observed above 250°C in these samples that are devoid of greigite.

In contrast, almost all of the greigite-dominated samples carry a large reversed polarity component up to 300°C or higher that is only occasionally overprinted by a small normal polarity component at the lowest temperature steps. The greigite population thus carries a stable reversed signal. There is a large deviation of the mean declination from South (Figure 12, 70.8° and 64.2° for tectonic and in situ coordinates, respectively). This indicates a tectonic anticlockwise rotation of ∼65° after the acquisition of the magnetization. The time interval in which the tectonic rotation must have occurred can only be estimated by using some first-order approximations. The normal polarity VRM components do not show rotation, implying that rotation predates the base of the Bruhnes chron at 0.78 Ma. The greigite nodules acquired their remanence in a reversed polarity interval, based on their inclination. The top of the section is biostratigraphically dated at anywhere between 3.33 and 1.88 Ma (Chron C2n) [Tate et al., 2014]. Therefore, the age of the onset of rotation is 3.33 Ma or younger.

7. Implications, Prospects, and Conclusion

We aimed to solve greigite-related remanence problems using the IRM-acquisition end-member model as a potential new extra tool. For both sections, the end-member model and the rock magnetic research in combination with SEM-observations have successfully assessed the veracity of the NRM residing in both greigite and magnetite. Application of these findings to the paleomagnetic data set of the Viqueque Type section enabled the allocation of quality labels to the NRM-components. This procedure resulted in a meaningful integrated bio-magnetostratigraphic age model for the Viqueque Type section. The minimum age for the

top of the section equals the top of the Kaena subchron (C2An.1r). The two older polarity zones are identi-fied as subchrons C2An.2n and C2An.2r (Mammoth) of the Gauss Chron. This correlation implies a fairly uni-form sedimentation rate of ~80 cm/kyr for the interval above 43 m. Importantly, our analysis shows that the top of the section, of which age was biostratigraphically only constrained to 3.12–1.88 Ma, cannot be younger than the Kaena subchron, i.e., ~3.032 Ma.

The Cailaco River section contains a remagnetized greigite signal of late diagenetic origin as revealed by the microscopy. Therefore, it is impossible to establish a meaningful magnetostratigraphy. A significant counterclockwise tectonic rotation of ~65° of the section, however, could be determined for this section, which must have occurred after secondary greigite growth sometime in the late Pliocene or Quarternary.

Do these results make the end-member modeling of IRM-acquisition curves the "holy grail" of paleomag-netic methods to diagnose remagnetizations? Unfortunately not, because the end-member model approach is not stand-alone. Its interpretation must be supported by other rock magnetic methods and (electron) microscopy to produce a proper translation of the end-member into magnetic minerals. End-member modeling is, however, a first and very important step in the interpretation process. Its asset is threefold: (1) it provides the possibility to compare all samples in a section, (2) it identifies the samples with the most extreme end-member contributions, and (3) it enables to extrapolate rock magnetic properties determined on a subset of samples to the remaining samples in a section. The follow-up rock magnetic research and related microscopy study can therefore be tailored and focused.

Further, microscopic research is crucial for the final interpretation of the end-members, especially for grei-gite. As shown in the present study, rock magnetic properties by themselves cannot constrain the origin of greigite to a unique formation process. So, not only thermoviscous resetting cannot be diagnosed by end-member modeling (because the grain size population remains the same), but also different modes of occur-rence of greigite should be dealt with cautiously. Their formation process must be interpreted with an inte-grated approach of end-member modeling, complementing rock magnetic data, and microscopic observations. Where possible, the paleomagnetic data itself should be included as well.

Besides its role as reference frame, the end-member model can be highly valuable in linking the recognized magnetic mineral suites to their formation processes. As shown in this work, the greigite and magnetite suites in the Viqueque Type section are closely related to each other via a single diagenetic process. To some degree, this emerges from the end-members models as well: in models with a high number of end-members those end-members are mixtures of these two magnetic mineral suites.

When dealing with inconsistent polarity patterns in greigite sediments, the mere recognition of greigite is not sufficient; the most important step is to evaluate the timing of diagenesis and remanence acquisition. This research has shown that rock magnetic and microscopic observations are able to do so without strong reliance on paleomagnetic field tests (e.g., fold tests, inclination shallowing tests). The end-member model-ing of IRM-acquisition curves is thus most useful as reference frame for the unraveling of complex greigite-related remanence problems.

References

Aubourg, C., J. P. Pozzi, and M. Kars (2012), Burial, claystones remagnetization and some consequences for magnetostratigraphy, *Geol. Soc. Spec. Publ.*, *371*, 181–188.

Audley-Charles, M. G. (1986), Rates of Neogene and quarternary tectonic movements in the Southern Banda Arc based on micropaleontol-ogy, *J. Geol. Soc. London*, *143*, 161–175.

Audley-Charles, M. G. (2011), Tectonic post-collision processes in Timor, *Geol. Soc. Spec. Publ.*, *355*(1), 241–266.

Bazylinski, D., R. B. Frankel, B. R. Heywood, S. Mann, J. W. King, L. Donaghay, and A. K. Hanson (1995), Controlled biomineralization of mag-netite (Fe_3O_4) and greigite (Fe_3S_4) in a magnetotactic bacterium, *Appl. Environ. Microbiol.*, *61*(9), 3232–3239.

Benning, L. G., R. T. Wilkin, and H. L. Barnes (2000), Reaction pathways in the Fe–S system below 100°C, *Chem. Geol.*, *167*, 25–51.

Berner, R. A. (1984), Sedimentary pyrite formation: An update, *Geochim. Cosmochim. Acta*, *48*, 605–615.

Canfield, D. E., R. Raiswell, and S. Bottrell (1992), The reactivity of sedimentary iron minerals toward sulfide, *Am. J. Sci.*, *292*, 659–683.

Carter, D. J., M. G. Audley-Charles, and A. J. Barber (1976), Stratigraphical analysis of island arc—Continental margin collision in eastern Indonesia, *J. Geol. Soc. London*, *132*, 179–198.

De Smet, M. E., A. R. Fortuin, S. R. Troelstra, L. J. van Marle, M. Karmini, S. Tjokrosapoetro, and S. Hadiwasastra (1990), Detection of collision-related vertical movements in the Outer Banda Arc (Timor, Indonesia), using micropaleontological data, *J. Southeast Asian Earth Sci.*, *4*, 337–356.

Day, R., M. Fuller, and V. A. Schmidt (1977), Hysteresis properties of titanomagnetites: grain-size and compositional dependence, *Phys. Earth Planet. Inter.*, *13*, 260–267.

Dekkers, M. J. (2012), End-member modelling as an aid to diagnose remagnetization: A brief review, *Geol. Soc. Spec. Publ.*, *371*, 253–269.

Duffy, B., M. C. Quigley, R. A. Harris, and U. Ring (2013), Arc-parallel extrusion of the Timor sector of the Banda arc-continent collision, *Tectonics*, *32*, 641–660.

Dunlop, D. J. (2002), Theory and application of the Day plot (Mrs/Ms vs. Hcr/Hc) 1, Theoretical curves and tests using titanomagnetite data, *J. Geophys. Res.*, *107*(B3), 1–22.

Fichtner, A., M. de Wit, and M. van Bergen (2010), Subduction of continental lithosphere in the Banda Sea region: Combining evidence from full waveform tomography and isotope ratios, *Earth Planet. Sci. Lett.*, *297*(3–4), 405–412.

Florindo, F., and L. Sagnotti (1995), Palaeomagnetism and rock magnetism in the upper Pliocene Valle Ricca (Rome, Italy) section, *Geophys. J. Int.*, *123*(2), 340–354.

Fu, Y., T. von Dobeneck, C. Franke, D. Heslop, and S. Kasten (2008), Rock magnetic identification and geochemical process models of greigite formation in Quaternary marine sediments from the Gulf of Mexico (IODP Hole U1319A), *Earth Planet. Sci. Lett.*, *275*(3–4), 233–245.

Giovanoli, F. (1979), *Die Remanente Magnetisierung von Seesedimenten*, 201 pp., Univ. Zuerich, Zurich, Switzerland.

Gong, Z., M. J. Dekkers, D. Heslop, and T. A. T. Mullender (2009), End-member modelling of isothermal remanent magnetization (IRM) acquisition curves: A novel approach to diagnose remagnetization, *Geophys. J. Int.*, *178*(2), 693–701.

Haig, D. W. (2012), Palaeobathymetric gradients across Timor during 5.7–3.3 Ma (latest Miocene–Pliocene) and implications for collision uplift, *Palaeogeogr. Palaeoclimatol. Palaeoecol.*, *331–332*, 50–59.

Haig, D. W., and E. McCartain (2007), Carbonate pelagites in the post-Gondwana succession (Cretaceous–Neogene) of East Timor, *Aust. J. Earth Sci.*, *54*(6), 875–897.

Harris, R. A. (1991), Temporal distribution of strain in the active Banda Orogen. A reconciliation of rival hypotheses, *J. Southeast Asian Earth Sci.*, *6*, 373–386.

Harris, R. A. (1992), Peri collisional extension and the formation of Oman type ophiolites in the Banda Arc and Brooks Range, *Geol. Soc. Spec. Publ.*, *60*, 301–325.

Harris, R. A. (2006), Rise and fall of the eastern Great Indonesian Arc recorded by the assembly dispersion and accretion of the Banda Terrane, Timor, *Gondwana Res.*, *10*, 207–231.

Harris, R. A. (2011), The nature of the banda arc-continent collision in the Timor region, in *Arc-Continent Collision, Frontiers in Earth Sciences*, edited by D. Brown and P. D. Ryan, pp. 163–211, Springer, Berlin Heidelberg.

Harris, R. A., R. K. Sawyer, and M. G. Audley-Charles (1998), Collisional melange development: Geologic associations of active melange-forming processes with exhumed melange facies in the western Banda orogen, Indonesia, *Tectonics*, *17*(3), 458–479.

Heslop, D., and M. Dillon (2007), Unmixing magnetic remanence curves without a priori knowledge, *Geophys. J. Int.*, *170*(2), 556–566.

Heslop, D., G. McIntosh, and M. J. Dekkers (2004), Using time- and temperature-dependent Preisach models to investigate the limitations of modelling isothermal remanent magnetization acquisition curves with cumulative log Gaussian functions, *Geophys. J. Int.*, *157*(1), 55–63.

Heywood, B. R., D. A. Bazylinski, A. Garratt-Reed, S. Mann, and R. B. Frankel (1990), Controlled biosynthesis of greigite (Fe_3S_4) in magnetotactic bacteria, *Naturwissenschaften*, *77*(11), 536–538.

Hilgen, F. J., L. J. Lourens, and J. A. van Dam (2012), The Neogene period, in *The Geologic Time Scale*, edited by F. M. Gradstein et al., pp. 923–978, Elsevier, Oxford, U. K.

Hüsing, S. K., M. J. Dekkers, C. Franke, and W. Krijgsman (2009), The Tortonian reference section at Monte dei Corvi (Italy): Evidence for early remanence acquisition in greigite-bearing sediments, *Geophys. J. Int.*, *179*(1), 125–143.

Jiang, W. T., C. S. Horng, A. P. Roberts, and D. R. Peacor (2001), Contradictory magnetic polarities in sediments and variable timing of neoformation of authigenic greigite, *Earth Planet. Sci. Lett.*, *193*(1–2), 1–12.

Just, J., D. Heslop, T. von Dobeneck, T. Bickert, M. J. Dekkers, T. Frederichs, I. Meyer, and M. Zabel (2012a), Multi-proxy characterization and budgeting of terrigenous end-members at the NW African continental margin, *Geochem. Geophys. Geosyst.*, *13*, Q0AO01, doi:10.1029/2012GC004148.

Just, J., M. J. Dekkers, T. von Dobeneck, A. van Hoesel, and T. Bickert (2012b), Signatures and significance of aeolian, fluvial, bacterial and diagenetic magnetic mineral fractions in Late Quaternary marine sediments off Gambia, NW Africa, *Geochem. Geophys. Geosyst.*, *13*, Q0AO02, doi:10.1029/2012GC004146.

Kao, S. J., C. S. Horng, A. P. Roberts, and K. K. Liu (2004), Carbon–sulfur–iron relationships in sedimentary rocks from southwestern Taiwan: Influence of geochemical environment on greigite and pyrrhotite formation, *Chem. Geol.*, *203*(1–2), 153–168.

Krs, M., F. Novak, M. Krsova, P. Pruner, and J. Jansa (1992), Magnetic properties and metastability of greigite-smythite mineralization in brown-coal basins of the Krusné hory Piedmont, Bohemia, *Phys. Earth Planet. Inter.*, *70*, 273–287.

Kruiver, P. P., M. J. Dekkers, and D. Heslop (2001), Quantification of magnetic coercivity components by the analysis of acquisition curves of isothermal remanent magnetisation, *Earth Planet. Sci. Lett.*, *189*, 269–276.

Lowrie, W. (1990), Identification of ferromagnetic minerals in a rock by coercivity and unblocking temperature properties, *Geophys. Res. Lett.*, *17*(2), 159–162.

Lucifora, S., F. Cifelli, M. Mattei, L. Sagnotti, D. Cosentino, and A. P. Roberts (2012), Inconsistent magnetic polarities in magnetite- and greigite-bearing sediments: Understanding complex magnetizations in the late Messinian in the Adana Basin (southern Turkey), *Geochem. Geophys. Geosyst.*, *13*, Q10002, doi:10.1029/2012GC004248.

Mann, S., N. H. C. Sparks, R. B. Frankel, D. A. Bazylinski, and H. W. Jannasch (1990), Biomineralization of ferrimagnetic greigite (Fe_3S_4) and iron pyrite (FeS_2) in a magnetotactic bacterium, *Nature*, *343*, 258–261.

McCabe, C., R Van Der Voo, D. R. Peacor, C. R. Scotese, and R. Freeman (1983), Diagenetic magnetite carries ancient yet secondary remanence in some Paleozoic sedimentary carbonate, *Geology*, *11*(4), 221–223.

McFadden, P. L. (1990), A new fold-test for palaeomagnetic studies, *Geophys. J. Int.*, *103*, 163–169.

Meijers, M. J. M., D. J. J. van Hinsbergen, M. J. Dekkers, D. Altıner, N. Kaymakcı, and C. G. Langereis (2011), Pervasive Palaeogene remagnetization of the central Taurides fold-and-thrust belt (southern Turkey) and implications for rotations in the Isparta Angle, *Geophys. J. Int.*, *184*(3), 1090–1112.

Mullender, T. A. T., A. J. van Velzen, and M. J. Dekkers (1993), Continuous drift correction and separate identification of ferrimagnetic and paramagnetic contributions in thermomagnetic runs, *Geophys. J. Int.*, *114*(3), 663–672.

Nguyen, N., B. Duffy, J. Shulmeister, and M. Quigley (2013), Rapid Pliocene uplift of Timor, *Geology*, *41*(2), 179–182.

Quigley, M. C., B. Duffy, J. Woodhead, J. Hellstrom, L. Moody, T. Horton, J. Soares, and L. Fernandes (2012), U/Pb dating of a terminal Pliocene coral from the Indonesian Seaway, *Mar. Geol.*, *311–314*, 57–62.

Roberts, A. P., and B. J. Pillans (1993), Rock magnetism of lower/middle Pleistocene marine sediments, Wanganui Basin, New Zealand, *Geophys. Res. Lett.*, *20*(9), 839–842.

Roberts, A. P., and R. Weaver (2005), Multiple mechanisms of remagnetization involving sedimentary greigite (Fe₃S₄), *Earth Planet. Sci. Lett.*, *231*(3–4), 263–277.

Roberts, A. P., W. T. Jiang, F. Florindo, C. S. Horng, and C. Laj (2005), Assessing the timing of greigite formation and the reliability of the Upper Olduvai polarity transition record from the Crostolo River, Italy, *Geophys. Res. Lett.*, *32*, L05307, doi:10.1029/2004GL022137.

Roberts, A. P., L. Chang, C. J. Rowan, C. S. Horng, and F. Florindo (2011), Magnetic properties of sedimentary Greigite (Fe₃S₄): An update, *Rev. Geophys.*, *49*, RG1002, doi:10.1029/2010RG000336.

Roosmawati, N., and R. A. Harris (2009), Surface uplift history of the incipient Banda arc continent collision: geology and synorogenic foraminifera of Rote and Savu Islands, Indonesia, *Tectonophysics*, *479*, 95–110.

Rowan, C. J., and A. P. Roberts (2006), Magnetite dissolution, diachronous greigite formation, and secondary magnetizations from pyrite oxidation: Unravelling complex magnetizations in Neogene marine sediments from New Zealand, *Earth Planet. Sci. Lett.*, *241*(1–2), 119–137.

Rowan, C. J., A. P. Roberts, and T. Broadbent (2009), Reductive diagenesis, magnetite dissolution, greigite growth and paleomagnetic smoothing in marine sediments: A new view, *Earth Planet. Sci. Lett.*, *277*(1–2), 223–235.

Sagnotti, L., A. P. Roberts, R. Weaver, K. L. Verosub, F. Florindo, C. R. Pike, T. Clayton, and G. S. Wilson (2005), Apparent magnetic polarity reversals due to remagnetization resulting from late diagenetic growth of greigite from siderite, *Geophys. J. Int.*, *160*(1), 89–100.

Snowball, I. F., and R. Thompson (1988), The occurrence of greigite in sediments from Loch Lomond, *J. Quat. Sci.*, *3*(2), 121–125.

Snowball, I. F., and R. Thompson (1990a), A mineral magnetic study of Holocene sedimentation in Lough Catherine, Northern Ireland, *Boreas*, *19*(2), 127–146.

Snowball, I. F., and R. Thompson (1990b), A stable chemical remanence in Holocene sediments, *J. Geophys. Res. Lett.*, *95*(B4), 4471–4479.

Spakman, W., and R. Hall (2010), Surface deformation and slab–mantle interaction during Banda arc subduction rollback, *Nat. Geosci.*, *3*(8), 562–566.

Standley, C. E. and R. A. Harris (2009), Tectonic evolution of forearc napes of the active Banda arc-continent collision: Origin, age, metamorphic history and structure of the Lolotoi Complex, East Timor, *Tectonophysics*, *479*(1-2), 66–94.

Tate, G. W., et al. (2014), Resolving spatial heterogeneities in exhumation and surface uplift in Timor-Leste: constraints on deformation processes in young orogens, *Tectonics*, doi:10.1002/2013TC003436.

Tauxe, L., K. P. Kodama, and D. V. Kent (2008), Testing corrections for paleomagnetic inclination error in sedimentary rocks: A comparative approach, *Phys. Earth Planet. Inter.*, *169*(1–4), 152–165.

Van Der Voo, R., and T. H. Torsvik (2012), The history of remagnetization of sedimentary rocks: deceptions, developments and discoveries, *Geol. Soc. Spec. Publ.*, *371*, 23–53, doi:10.1144/SP371.2.

Van Dongen, B. E., A. P. Roberts, S. Schouten, W.-T. Jiang, F. Florindo, and R. D. Pancost (2007), Formation of iron sulfide nodules during anaerobic oxidation of methane, *Geochim. Cosmochim. Acta*, *71*, 5155–5167.

Van Hinsbergen, D. J. J., M. J. Dekkers, and A. Koç (2010), Testing Miocene remagnetization of Bey Daglari: Timing and amount of Neogene rotations in SW Turkey, *J. Turk. Earth Sci.*, *19*, 123–156.

Van Velzen, A. J., and J. D. Zijderveld (1995), Effects of weathering on single-domain magnetite in Early Pliocene marine marls, *Geophys. J. Int.*, *121*, 267–278.

Vandamme, D. (1994), A new method to determine paleosecular variation, *Phys. Earth Planet. Inter.*, *85*(1–2), 131–142.

Vasiliev, I., M. J. Dekkers, W. Krijgsman, C. Franke, C. G. Langereis, and T. A. T. Mullender (2007), Early diagenetic greigite as a recorder of the palaeomagnetic signal in Miocene-Pliocene sedimentary rocks of the Carpathian foredeep (Romania), *Geophys. J. Int.*, *171*(2), 613–629.

Vasiliev, I., C. Franke, J. D. Meeldijk, M. J. Dekkers, C. G. Langereis, and W. Krijgsman (2008), Putative greigite magnetofossils from the Pliocene epoch, *Nat. Geosci.*, *1*(11), 782–786.

Wade, B. S., P. N. Pearson, W. A. Berggren, and H. Paelike (2011), Review and revision of Cenozoic tropical planktonic foraminiferal biostratigraphy and calibration to the geomagnetic polarity and astronomical time scale, *Earth Sci. Rev.*, *104*, 111–142.

Weltje, G. J. (1997), End-member modelling of compositional data: Numerical-statistical algorithms for solving the explicit mixing problem, *Math. Geol.*, *29*(4), 503–549.